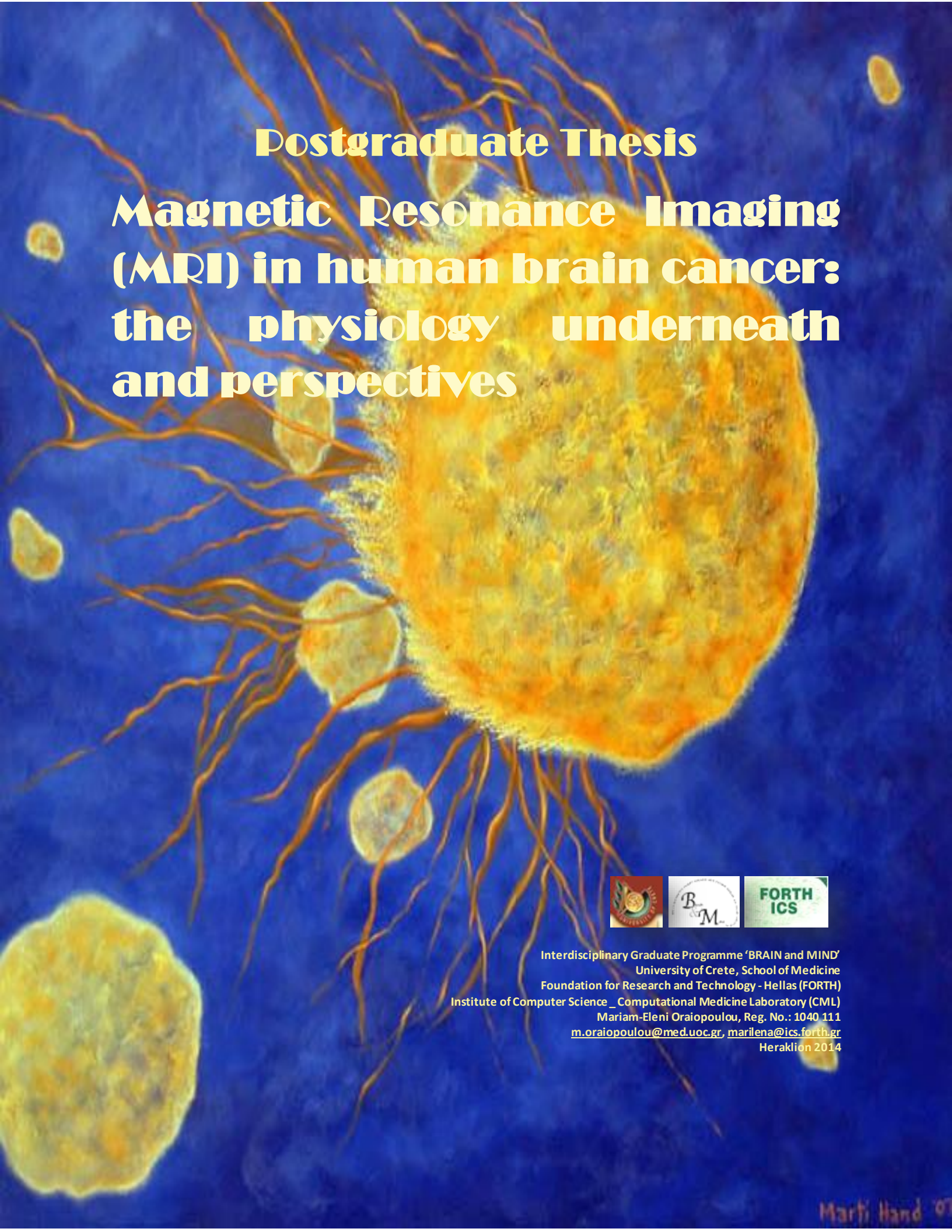

Postgraduate Thesis

Magnetic Resonance Imaging (MRI) in human brain cancer: the physiology underneath and perspectives

Interdisciplinary Graduate Programme 'BRAIN and MIND'
University of Crete, School of Medicine
Foundation for Research and Technology - Hellas (FORTH)
Institute of Computer Science _ Computational Medicine Laboratory (CML)
Mariam-Eleni Oraiopoulou, Reg. No.: 1040 111
m.oraiopoulou@med.uoc.gr, marilena@ics.forth.gr

Heraklion 2014

THESIS SUPERVISOR

Marias Kostas, Ph.D., Principal Researcher

Interdisciplinary Graduate Programme in the Brain and Mind Sciences,

Foundation for Research & Technology – Hellas (FORTH),

Institute of Computer Science, Laboratory of Computational Medicine, Heraklion, Greece
kmarias@ics.forth.gr

EVALUATORS

Sakkalis Vangelis, Ph.D., Principal Researcher

Interdisciplinary Graduate Programme in the Brain and Mind Sciences,

Foundation for Research & Technology – Hellas (FORTH),

Institute of Computer Science, Laboratory of Computational Medicine, Heraklion, Greece
sakkalis@ics.forth.gr

Ioannis Charalampopoulos, Assistant Professor of Pharmacology

Interdisciplinary Graduate Programme in the Brain and Mind Sciences,

Dept. of Basic Sciences, Laboratory of Pharmacology,

Faculty of Medicine, University of Crete, Heraklion, Greece
gharalab@med.uoc.gr

ABSTRACT

Cancer cells in solid tumors form a mass with augmented metabolic needs due to constant vigorous changes. As the solid tumor develops, it must generate its own blood supply due to insufficient diffusion of nutrients and oxygen from pre-existing vasculature. Intra-tumoral hypoxia is considered to be the main driving force of induced angiogenesis within the tumor in agreement with Folkman's assertion. Hypoxia-inducible factor (HIF-1α) is a transcription factor that promotes ischemia-driven angiogenesis through the induction of differential expression of the vascular endothelial growth factor (VEGF). VEGF appears to be a key-molecule for both the pro-angiogenic events and the survival of newly formed vessels [1]. In general, aspects such as cell proliferation and invasion, angiogenic net rates, oxygen consumption and vasculature have been approved to be fundamental for shaping the cancer in a heterogeneous and compartmentalized tumor mass.

High grade (astrocytic) gliomas and particularly glioblastoma multiforme (GBM), are known to have a prominence of vasculature and appear to be among the most common brain cancers. In addition, as an extreme malignant form of cancer in conjunction with its special features, the importance of early diagnosis and effective treatment options make evident the need for exploitation and improvement of the imaging techniques. Imaging techniques such as dynamic contrast enhanced magnetic resonance imaging (DCE-MRI) with the administration of a Gd-based contrast agent (GBCA) are used for diagnosis and characterization of GBM. Studies correlating imaging biomarkers with clinical outcome are of great interest.

The work is comprised of two parts:

First, a feasibility study is performed using DCE-MRI in order to provide patient-specific input to a proliferation-invasion- hypoxia- necrosis- angiogenesis (PIHNA) model. This work focuses on correlating pharmacokinetic (PK)-based imaging biomarkers to underlying biological phenomena regarding vasculature composition of the tumor. The assumptions made represent novel work in this direction. Feasibility results of applying the tumor growth model to real clinical cases are presented, accompanied by a study of the effect of changing certain model parameters on the pattern of the simulated tumor.

Second, an examination of the tracer's kinetics in DCE-MRI has been made in order to assess the vessel leakage through the estimation of the transfer and disposition of GBCAs in a putative lesion. In this case, a physiologically-based pharmacokinetic (PBPK) model was used through the application of Simcyp® simulator platform to assess *in silico* the disposition of pharmacologic agents in the body. A whole-body PBPK approach is presented evaluating the impact of vasculature in the extravascular-extracellular disposition of Gd-DTPA (Gadopentetic acid, Magnevist®) in a brain tumor lesion.

The aim of this work in overall is to shed light in the interconnections between imaging biomarkers and related mechanisms and molecules, focusing mainly on the effect of vasculature. In other words, to find a way of translating MRI biomarkers to biologically significant phenotype and brain tumor physiology.

ΠΕΡΙΛΗΨΗ

Τα καρκινικά κύτταρα στους συμπαγείς όγκους διαμορφώνουν μία μάζα με αυξημένες μεταβολικές ανάγκες εξαιτίας των συνεχών και έντονων μεταβολών. Καθώς αναπτύσσεται ο συμπαγής αυτός όγκος, πρέπει να δημιουργήσει τη δική του αιματική παροχή εξαιτίας της ανεπαρκούς διάχυσης θρεπτικών και οξυγόνου από την προ-υπάρχουσα αγγείωση. Η υποξία εντός του όγκου θεωρείται η κύρια κινητήρια δύναμη για την επαγομένη αγγειογένεση στον όγκο σε συμφωνία με τον ισχυρισμό του Folkman. Ο επαγόμενος λόγω υποξίας παράγοντας HIF-1α είναι ένας μεταγραφικός παράγοντας που προάγει την αγγειογένεση λόγω ισχαιμίας μέσω της επαγωγής διαφορικής έκφρασης του αγγειακού ενδοθηλιακού αυξητικού παράγοντα (VEGF). Ο VEGF φαίνεται να είναι ένα μόριο-κλειδί τόσο για τα προ-αγγειογενετικά γεγονότα όσο και για την επιβίωση των νεοσχηματισμένων αιμοφόρων αγγείων [1]. Γενικά, θέματα όπως ο κυτταρικός πολλαπλασιασμός και η εισβολή, τα καθαρά ποσοστά αγγειογενετικών παραγόντων, η κατανάλωση οξυγόνου και η αγγείωση έχουν αποδειχθεί θεμελιώδη για το σχηματισμό του καρκίνου σε μία ετερογενή και διαμερισματοποιημένη καρκινική μάζα.

Τα υψηλού βαθμού (αστροκυτταρικά) γλοιώματα, και συγκεκριμένα το πολύμορφο γλοιβλάστωμα (GBM), είναι γνωστό ότι έχουν εκτεταμένη αγγείωση και φαίνονται να είναι ανάμεσα στους πιο κοινούς καρκίνους του εγκεφάλου. Επιπρόσθετα, ως μία ιδιαίτερα κακοήθης μορφή καρκίνου σε συνδυασμό με τα ειδικά χαρακτηριστικά του, η σημασία της έγκαιρης διάγνωσης και των αποτελεσματικών θεραπευτικών επιλογών καθιστούν εμφανή την ανάγκη για αξιοποίηση και βελτίωση των απεικονιστικών τεχνικών. Οι απεικονιστικές τεχνικές, όπως η δυναμικής αντίθεσης ενισχυμένη απεικόνιση μαγνητικού συντονισμού (DCE-MRI) με τη χορήγηση ενός σκιαγραφικού μέσου με βάση το γαδολίνιο (GBCA), χρησιμοποιούνται για τη διάγνωση και το χαρακτηρισμό του GBM. Μελέτες που συσχετίζουν απεικονιστικούς βιοδείκτες με κλινική έκβαση συγκεντρώνουν μεγάλο ενδιαφέρον.

Η εργασία αποτελείται από δύο μέρη:

Πρώτον, μία μελέτη σκοπιμότητας εκπονείται χρησιμοποιώντας τη DCE-MRI έτσι ώστε να παρέχονται δεδομένα εισόδου ειδικά για τον ασθενή σε ένα μοντέλο πολλαπλασιασμού- εισβολής- υποξίας- νέκρωσης- αγγειογένεσης (PIHNA). Αυτή η δουλειά επικεντρώνεται στο να παραβάλει απεικονιστικούς βιοδείκτες βασισμένους σε φαρμακοκινητική (PK) με υποκείμενα βιολογικά φαινόμενα σε σχέση με τη σύσταση του όγκου ως προς το αγγειακό σύστημα. Οι παραδοχές που γίνονται αντιπροσωπεύουν νέο έργο προς αυτή την κατεύθυνση. Ενδεικτικά αποτελέσματα της εφαρμογής του μοντέλου ανάπτυξης του όγκου σε πραγματικά κλινικά περιστατικά παρουσιάζονται, συνοδευμένα από μία έρευνα της επίδρασης της μεταβολής ορισμένων παραμέτρων του μοντέλου κατά το πρότυπο της προσομοίωσης του όγκου.

Δεύτερον, εξετάσθηκε ο έλεγχος της κινητικής του ιχνηθέτη στη DCE-MRI προκειμένου να εκτιμηθεί η διαρροή των αγγείων, μέσω του υπολογισμού της μεταφοράς και διάθεσης των GBCA σε μια υποθετική βλάβη. Σε αυτή την περίπτωση, ένα φαρμακοκινητικό μοντέλο με βάση τη φυσιολογία (PBPK) χρησιμοποιήθηκε μέσω της εφαρμογής της πλατφόρμας προσομοίωσης Simcyp®, για να εκτιμηθεί *in silico* η διάθεση των φαρμακολογικών παραγόντων στο σώμα. Παρουσιάζεται μία PBPK προσέγγιση σε ολόκληρο το σώμα η οποία αξιολογεί τον αντίκτυπο του αγγειακού κλάσματος στον εξωαγγειακή-εξωκυτταρική εναπόθεση του Gd-DTPA (Gadopentetic acid, Magnevist®) σε μία καρκινική βλάβη του εγκεφάλου.

Ο σκοπός αυτής της εργασίας συνολικά είναι να ρίξει φως στις διασυνδέσεις μεταξύ των απεικονιστικών βιοδεικτών και των συνδεόμενων μηχανισμών και μορίων, επικεντρωνόμενη κυρίως στην επίδραση του αγγειακού συστήματος. Με άλλα λόγια, να βρει ένα τρόπο ώστε να μεταφράσει τους MRI βιοδείκτες σε βιολογικά σημαντικούς φαινότυπους και στη φυσιολογία του όγκου του εγκεφάλου.

CONTENTS

1. GLIOMAS AND GLIOBLASTOMA MULTIFORME (GBM)

Of all human cancers, brain tumors represent the 1.4%, while brain is the second most common organ where cancer arises in children. Gliomas are among the most common (~40%) type of primary solid tumors that originate in the Central Nervous System (CNS). Gliomas' peak incidence is considered to be around the age of 60 years old , affecting ~40% more males than females [3]. They also represent up to 80% of cases of malignant brain tumors [4].They are found both in the brain and the spinal cord. The term 'glioma' refers to any tumor that derives from tissues of the brain other than nerve cells and blood vessels, such is glial cells. Glial cells are supportive cells in the neural system. In adults, they are unable of proliferation and thus, tumors are thought to derive most plausibly from multipotent progenitor cells (glial precursors and/or neural stem cells), showing histological features similar to astrocytes or oligodendroglial cells [3]. The initial population of the developing cancer mass is usually near the vascular niches [5, 6]. The vast majority of gliomas arise from astrocytes [3].

According to the World Health Organization (WHO), gliomas can be categorized in four grades (I-IV) based on cell type, anaplasia levels and malignancy [2]. Grades I and II are also characterized as low grade gliomas, with better prognosis for the patient and lower rate of proliferation, while III and IV are considered high-grade gliomas (Table 1). Low-grade gliomas may transit to high-grade through anaplasia. Poor prognosis of gliomas can be linked to the fact that by the time the lesion is visible and the symptoms have accumulated, the tumor has already been formed [5].

Table 1 GRADE CLASSIFICATION (I-IV) FOR ASTROCYTIC TUMORS OF THE CENTRAL NERVOUS SYSTEM ACCORDING TO WHO (ADOPTED FROM [2])

Astrocytic tumours	I	II	III	IV
Subependymal giant cell astrocytoma	•			
Pilocytic astrocytoma	•			
Pilomyxoid astrocytoma		•		
Diffuse astrocytoma		•		
Pleomorphic xanthoastrocytoma		•		
Anaplastic astrocytoma			•	
Glioblastoma				•
Giant cell glioblastoma				•
Gliosarcoma				•

RATIONALE

Half of the primary parenchymal tumors in the brain refer to glioblastoma multiforme (GBM) -classified in the latter category of gliomas along with diffusive astrocytoma- which also represents the ~20% of all primary intracranial tumors. Penetration into brain parenchyma differentiates GBM from malignant meningioma. GBM is considered to be an end-stage disease. GBM belongs in astrocytomas, a glioma arising from astrocytic cells [3].

The main characteristics of this tumor of the neuro-epithelial tissue are the cellular polymorphism, brisk mitotic activity, microvascular proliferation and necrosis. Distinguish between low and high grade gliomas

(i.e. GBM) are related with histological features such as intratumoral necrosis, angiogenesis, and cellular proliferation [3, 7]. Another typical GBM hallmark is the infiltrative nature of the peritumoral region edema. To this respect, white matter surrounding the lesion is affected and the edema is consisted of infiltrating tumor cells and a lesser proportion of vasculature [8, 9].

There is a theoretical classification of GBM into primary and secondary according to its appearance, development and malignancy, but not histology. As shown in some surveys, there is evidence for a differential genetic background, too. Primary GBM refers to a tumor mass which appears *de novo*, meaning without any pre-clinical or histological evidence of a previous low-grade astrocytoma that it derived from. In the MRI image of the primary glioblastoma central ischemic necrosis and advanced peritumoral edema are detected. Due to the lack of early diagnosis, this form is usually larger in size and more aggressive. As regards the secondary GBM, affecting mostly younger patients, it develops from a diffuse or anaplastic lower-grade astrocytoma which eventually evolves into GBM. Secondary GBM is a usual effect of recurrence after the resection of a less malignant, grade II lesion. Primary GBM seems to prevail in relation to the secondary epidemiologically, but not in response to therapy [3].

Surprisingly GBM enables to allocate extra-cranially. During the short time period of its development, some rare clinical cases of metastasis with GBM as the precursor lesion have been reported [10].

GBM is characterized by its specific features, the malignancy and the rapid progress. Time is the most critical factor because cognitive and functional deficits grow as a result of the expanding lesion. In addition, the only tool of GBM diagnosis and surveillance is imaging techniques and particularly MRI. Thus, the optimal scenario for patients with GBM and brain cancer in general is to find the right way of decoding MRI scans and obtain knowledge about the specific grade, the characteristics, the appropriate treatment and patients' response and probability of survival, all these from the very first moment that cancer is diagnosed. The last years, much effort is made in order to monitor therapeutic effect and tumor development with non-invasive imaging biomarkers.

HOW THE FUNCTIONALITY OF THE BRAIN IS AFFECTED?

The impairments and deficits that a brain tumor is responsible for may be attributed to the location that a tumor firstly appears and they consolidate and intensify as the tumor grows in stage. To be more specific, there is much difference between a tumor growing for example close to the lateral ventricle and one interpolating within the primary cortex. When the ventricle is adjacent to the tumor, there is enough space for the developed pressures and forces to be applied in a non-functional tissue portion and just compress the cerebral fluid inside the ventricle. In other words, if the tumor is located at a distance from a critical area, there is a delay before the symptoms firstly occur. These so called silent symptoms are usually found incidentally when a brain scan is done for another reason. Nevertheless, this is a controversial framework because despite the fact that the lack of symptoms is translated into quality of patient's life remaining better for a longer time, but the latency might specify a late stage or a weaker potential treatment response. On the contrast, when the tumor is expanded neighboring a region with an important role, the respective function is affected accordingly to the damage. Moreover, if the area has to do with a vital priority, the larger the lesion the more severe the pathology. In any case, besides the tumor mass itself growing, additional burden is imposed by the edema surrounding the tumor acting additively to intracranial pressure within the limited space.

There is narrow relative demographic literature as regards the anatomic origins of GBM. The most common locations that this kind of brain tumor is present are the hemispheric white matter tracts in general and mostly in the frontal and temporal lobes, as well as in the cerebellum [11, 12].

Symptoms are determined according to the structures and tissues affected. Alternatively, structural modifications lead to functional fluctuations. Symptoms become visible in a manner including headaches, nausea, vomiting and seizures. Otherwise functional problems, GBM usually may cause from subtle

personality changes and memory loss to muscle weakness and disturbances in vocalization and/or comprehension of speech.

The estimated prognosis for the glioblastoma is grim due to the high propensity, almost inevitable, for tumor recurrence and the duration of survival without treatment is estimated to be 4-7 months whereas a median survival of 12 to 15 months is expected following resection and/or adjuvant treatments and a 5 or 10 year survival estimated for the 3 and 1% of patients diagnosed with GBM, respectively [7, 13]. Glioblastoma is a highly vascularized tumor, recruiting pre-existed vessels of an already well oxygenated organ like brain and generating neo-vasculature from excessive levels of circulating vascular endothelial growth factor (VEGF) apart from other pro-angiogenic molecules [14].

2. TUMOR ANGIOGENESIS

Tissue function depends on sufficient and continuous supply of oxygen through blood vessels. To this respect, formed avascular tissues are provided with access to blood-vessel network by formation of arteries and veins through a process called angiogenesis (neo-vascularization). In most cases for normal (healthy) tissues, this process along with the underlying molecular mechanisms of pro- and anti-angiogenic molecules remains in balance [15]. This independent blood supply of the tumor mass is a process which continues during all the time period the cancer grows, spreads and matures.
On the other hand, the rate of cell growth in most malignant tumors is higher than the rate of vascular proliferation and formation. As tumor growth continues, the demands in oxygen and nutrients begin to exceed the blood supply and oxygen levels fall. This results in the appearance of hypoxic regions due to lack of oxygen diffusion even in tumor cells in nearby neovessels [16]. The resulted hypoxia activates the expression of hypoxic-inducible factors (HIF-1α, HIF-1β and HIF-2α) which trigger the expression of molecules such as VEGF, VEGFR1, VEGFR2, neuropilin-1, Ang2, nitric oxide synthase, TGFβ-1, PDGF-BB, endothelin-1, interleukin-8, IGF-II, Tie1, cyclooxygenase-2, etc. [17]. HIF-1a promotes mechanisms of angiogenesis (through VEGF) which in turn increases supply of oxygen and nutrients and enhance tumor growth till the blood supply becomes insufficient, which once more leads in appearance of hypoxic regions and a never-ending cycle of events from hypoxia and HIF-1α expression to VEGF, angiogenesis and tumor growth. In addition to the above, the mechanisms of angiogenesis in tumors fail to promote mature vascular networks and lead in formation of abnormal, leaky, with generally large pores and increased permeability, tortuous and/or shunt vessels, which fail to restore oxygen supply in hypoxic regions which further induces HIF expression (figure 1).

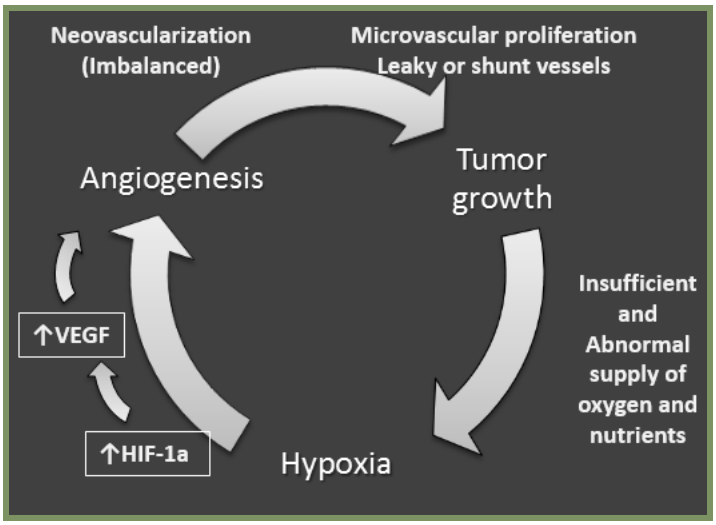

Figure 1_ *A never-ending cycle of events: tumor growth hypoxia and angiogenesis*

Immunohistochemical data from patients with high grade gliomas, and particularly GBM and other astrocytomas, relate the high levels of hypoxia as the grade of the cancer evolves to increased levels of HIF-1α and as a consequence, higher expression of VEGF (figure 2). This correlation is shown better around areas of necrosis and is distributed in the pseudopalisading cells which are located there [1].
At a cellular / tissue level, the series of events is a multi-step repeatable process. In brief, first, the pre-existing neighboring vessels stretch and expand towards tumor as a response to the pro-angiogenic factors released by cancer cells. The new endothelial cells migrate in a concrete way while degrading concurrently the extracellular matrix (ECM). After the vascular tube is formed and the tumor is partially oxygenated, support cells such as pericytes and fibroblasts are recruited in the periphery of the vessel and the tumor's microenvironment is regionally completed [17].

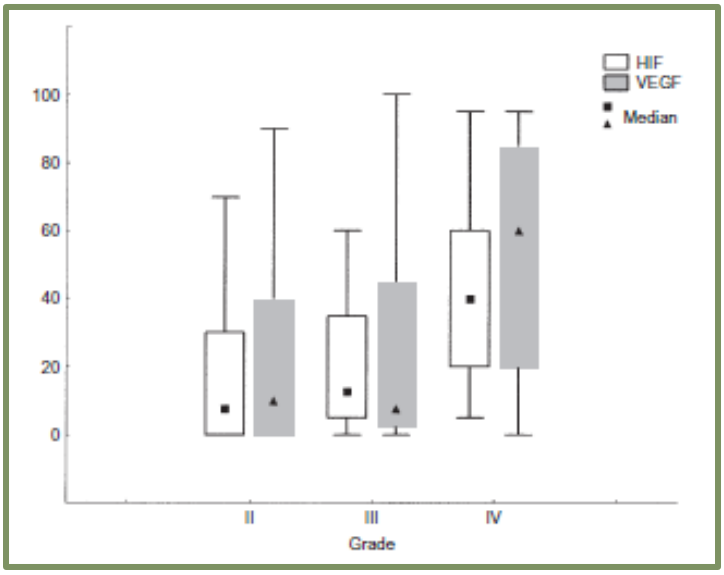

Figure 2_ *Graph illustrating the parallel increase of HIF-1$^{\alpha}$ and VEGF levels with up-grading histologically [1].*

MECHANISMS OF NEO-VASCULARIZATION [18]

The proliferative vessels are considered to be a hallmark of GBM. Till today, there have been described at least five mechanisms by which the formation of a vessel network is established in the growing tumor as regards gliomas (and not only), with hypoxia-related signaling to be involved in most of the cases. These mechanisms appear to take place in a rather not strict chronological order with a possibility of coexistence locally within the tumor. In addition, the term 'angiogenesis' mentioned above has to be redefined and replaced by the more general 'neo-vascularization' when referring to tumor's oxygenation mechanisms, as it appears to be the major mechanism for the tumor in order to achieve normoxia and satisfy the increased nutritional demands, but yet not the only one.
The initial step in the formation of vasculature is the one called 'vascular co-option', which refers to aggregation of tumor cells around the host-vasculature of the lesion. Angiopoietin-2 (ANG-2) appears to be the key-molecule depending on HIF-related mechanisms and in particular from HIF-1. Preceding induced VEGF levels, ANG-2 regulates the proliferation and migration of endothelial cells, whereas in VEGF shortage, ANG-2 promotes cell apoptosis and destabilizes the vessel network. Vascular co-option is usually observed in the periphery of the tumor mass and experimental data suggest that potentially reflects tumor areas where hypoxic and pro-angiogenic factors are stimulated due to obstruction of co-opted vessels.

Angiogenesis, as already mentioned, refers to the formation of new vessels from pre-existing ones. Molecules involved in this process are pro-angiogenic growth factors such as VEGF and molecules regulating the delta-Notch pathway. Additional role is attributed to matrix metalloproteinases (MMPs) with proteolytic facilitation and to integrins which implicate the final steps of vessel maturation.

Angiogenesis represents a major type of neovascularization and it is largely under hypoxia mechanisms control and especially HIF-1a. Mostly around the necrotic cores of the tumor, with minimized oxygen supply, the increased expression of HIF-1α activates the subsequent expression of the VEGF. In parallel with VEGF, there is also the hypoxia-related C-X-C chemokine receptor 4 (CXCR4)/ stromal-derived factor-1α (SDF-1α) pathway which further contributes in angiogenesis. On the other hand, the HIF-1α-mediated cascades appear to be hypoxia-independent in some cases. Glioma stem cells appear to produce pro-angiogenic factors like VEGF and SDF-1α, too.

As a final point, angiogenetic mechanisms of vascularization in tumors result in leaky, tortuous and abnormal vessels with irregularly increased permeability and fluid retention problems. The immatureness of the newly formed blood vessels may also explain the intensity of the blood brain barrier's (BBB) permeability and eventual breakdown. BBB results from the formation of an astrocytic sheath close to the basement membrane of the capillary endothelium. BBB works as a 'filter' between blood circulation and brain matter which selectively controls the advent of substances [3].

Vasculogenesis is another type of bloodstream development in tumors and is referred to the recruitment of the bone marrow-derived cells (BMDCs) in order to differentiate into either endothelial cells (endothelial progenitor cells, EPCs), macrophages (tumor-associated macrophages, TAMs) and possible to other cell types. This type of mechanism is deviated from HIF, although is driven by hypoxia-induced pathways, such as SDF-1α/CXCR4.

The last two cell-originated mechanisms, vascular mimicry and glioblastoma-endothelial cell transdifferentiation, show common morphological schemes on the tumor cells. In vascular mimicry, tumor cells themselves seem to be transformed in order to create vascular channels with blind ends and vessel properties. The role of hypoxia is questionable, but if accepted, then it is HIF-related. In transdifferentiation, the tumor cells appear to morphologically be engaged into endothelial-like cells and to form even more functional, tubular and vascular-like networks. This phenotype is also attributed to hypoxia and HIF-related pathways, with the role of GSCs under question. These two mechanisms appeared to be involved in cases treated with anti-VEGF therapy and showed resistance to it after an initial response [19].

3. IMAGING BIOMARKERS IN COMBINATION WITH BIOLOGICAL EVIDENCE FOR THE ASSESSMENT OF GBM PHYSIOLOGY AND TREATMENT EFFICACY

Imaging techniques such as MRI play an important role in clinical practice for cancer diagnosis and therapy monitoring. The field of *radiomics* aims to shed light in defining tumor heterogeneity in a non-invasive way. However, specific information concerning tumor mass can be given by histological analysis of the tissue and in particular molecular assays. These two approaches need to be effectively combined in order to be able to correspond imaging biomarkers to biological phenomena and conversely, molecular data to phenotypically differing tumors in MRI.
In the next lines some possible correlations and complementarity of molecular/imaging biomarkers are discussed.

Tumor type – diagnosis. While imaging information e.g. an MRI can be used for assisting diagnosis, the ultimate proof is given by histology and defining the type of the cancer in most cases requires molecular validation. Neither the detected lesion based on medical imaging nor just the identification of molecular biomarkers alone is enough for the accurate diagnosis of cancer [14]. The complementarity of these two worlds is already apparent in some cases, e.g. the specific tumor sites where biopsy material is taken from are usually defined by an MRI scan. Also, propensity for recurrence has to be thoroughly checked both with molecular analysis and imaging techniques.

Correct timing for treatment – treatment choice. The therapies chosen against cancer are a combination of scientific indication, method availability and medical experience. MRI measurements are related to tumor physiology, i.e. vasculature, cellularity, diffusion, etc. Depending on the target of the therapy, the timing, frequency/quantity are critical factors. Part of this information can be indirectly given from imaging studies such as MRI in an individualized fashion and can be complemented by molecular findings. For example, if the aim is to target vasculature, molecular evidence can lead to the correct choice between embolotherapy and vessels' corruption or anti-angiogenesis and vessels' maturation. It has been reported that tumor-cell originated neovascularization in GBM exhibits anti-angiogenic treatment resistance [14]. If molecular biomarkers of GBM-endothelial cell transdifferentiation are detected [18], then the present increased vascularity in MRI cannot be treated with anti-angiogenic drugs to help chemotherapy [20], since it would have minimal effect.

Prediction of response to therapy based on MRI data. What are the differences between the tissues? A biopsy can show differences in tumor compartments either on a tissue, cell or molecular level. For example, patients' stratification based on apparent diffusion coefficient (ADC) histogram analysis for response to anti-angiogenic treatment in GBM recurrence shows differences in extracellular matrix-related proteins [21]. In other words, tissue's rigidity and extracellular composition and not just cancer cells appear to play a critical role.

Therapies targeting substances. If the aim is to target a specific molecule, the detection and identification of the substance is crucial. For example, immunotherapy is meaningful when the immune cells are exposed to molecules that are particularly expressed from cancer cells in their surface or not. The choice and the effectiveness of the treatment can be evaluated from MRI scans [22].

Indications from MRI for necrosis. Necrosis for the majority of cancer types declares higher stages. If a molecular examination shows a high concentration of phospholipids, then the indications for necrosis will be confirmed. Alternatively, the region of necrosis can be anatomically specified by MR images. Magnetic resonance spectroscopy (MRS) and MRS Imaging (MRSI) are imaging techniques targeting this kind of information non-invasively, but with the compromise of poor spatial resolution. Also, the interplay of molecular/imaging biomarkers can be beneficial for the discrimination between tumor necrosis and

radiation necrosis. Characterization of other morphologically different regions, like peritumoral regions and edema or hypoxia, even differentiation between cancers [23] can also be based in such approaches.

In this front, DCE-MRI is able to approach the activity of the tumor based on vascular physiology and recent surveys show ability of discrimination between radiation necrosis and tumor recurrence, but with significant overlap between the two. For instance, in T2-weighted images, pure tumor necrosis is matched to the slowest rates of enhancement, while recurrent tumor owns the greatest mean maximal enhancement rates; mixed radiation necrosis and primary tumor have intermediate values [13].

Discrimination of tumor's stage. For example, tumor's invasive phase can probably be recognized through molecular markers, e.g. unattached molecules of the basal membrane, low cadherins concentration, etc. The proliferation rate and tumor progression can be assessed by MR images of different time points [24] and combined to such substances' detection, i.e. free molecules of basal membrane and/or suppression, i.e. low cadherins expressed by cancer cells.

Parameterizing tumor growth computational models. Emerging biomarkers from imaging modalities can be the input for simulated tumors, complemented by molecular information. The advantage of patient-specific initialization, standardization and validation of the model is the clinically valid outcome [25].

It is hard to distinguish whether the observed increase in brain tumor incidence is true or it is due to the recent technological progress in the diagnostic imaging [12]. MRI, conventional or not, is traditionally used as a non-invasive method for the evaluation of morphological and physiological features, so as tumor size and spatial recognition or tumor vasculature. Diffusion-Weighted MRI (DW-MRI) allows measuring the diffusion of water in the brain, which reflects the effective displacement of its molecules while migrating for a given time. It has the advantage of no need for intravenous contrast media and it is performed by several T2-weighted MRI scans acquired after appropriate sequencing. The maps illustrated with this type of MRI are those of apparent diffusion coefficient (ADC) and measurements in regions of lesion are compared to those of normal tissue. Different ADC values are indicative of cellularity, tissue disorganization and composition and density of extracellular space [26].
Following the same logic, Perfusion-Weighted (PW-MRI) describes the rate of nutrients and blood delivery via blood into brain tissue parenchyma. Hemodynamic parameters such is cerebral blood volume (CBV) are measured with the use of contrast agents -usually, gadolinium (Gd)-based. The maps that are constructed through this method indicate cerebral microvasculature and thus, the levels of angiogenesis and the grade of the tumor are visualized and evaluated [27]. DCE-MRI is used for the calculation of the vascular permeability constants through pharmacokinetic (PK) models and is a useful tool for characterizing tumor blood vessels and different compartments of the affected tissue.

As explained, the general idea followed by translating MRI data is to establish imaging biomarkers with predicting capabilities to therapies. In the next paragraph, knowledge regarding anti-angiogenic / anti-vascular therapy using MRI methodology is indicatively reported.

MRI FOR THE ASSESSMENT OF ANTI-ANGIOGENIC TREATMENT TARGETING VEGF

Bevacizumab is a monoclonal antibody targeting VEGFA [28] and used in the anti-angiogenic treatment under the trademark Avastin® (Genentech, 2004, drug label: http://www.accessdata.fda.gov/drugsatfda_docs/label/2009/125085s0169lbl.pdf).
Avastin is approved, apart from other types of cancer, for GBM and is received as a single agent or in combination with other chemotherapy (e.g. paclitaxel, a mitotic inhibitor drug) [28]. To be more specific, anti-VEGF treatment is approved for diseases such as lung, kidney, colorectal, breast cancer and high grade gliomas. Results from the Bevacizumab trials show obstruction of the VEGF pathway, reduction of

tumor perfusion, vascular volume, microvascular density, interstitial fluid pressure and the number of circulating mature and progenitor endothelial cells. Independent anti-angiogenic treatment, also known as monotherapy, produces limited clinical effects. Thus, it has been suggested to affect the tumor blood vessels so that facilitating chemotherapies in drug delivery and action and this is why the two therapies usually are combined [29]. There is also the idea that bevacizumab induces a significant anti-edemigenous effect by transiently normalizing the tumor vasculature and by restoring the BBB [30].

Despite the first hesitations about brain hemorrhage and proteinuria, patients with brain metastasis are now treated with bevacizumab depending on the primary tumor even as a maintenance therapy in some cases. So are those with recurrent glioblastoma [13] and primary high grade gliomas [31], too. Quality of life is gained, allowing the reduction of high-dose dexamethasone administration and delaying the whole-brain radiation therapy. Toxicity is observed rarely, but it is not completely absent [30].

It has been demonstrated that from DWI-MRI, ADC histogram analysis may be predictive of the response to Avastin in cases of either recurrent GBM and/or with GBM treated up-front- that is, before recurrence- with bevacizumab. ADC histogram analysis performed within the enhancing tumor regions can stratify patients with recurrent GBM into high- and low-risk groups [32]. Apart from that, a recent multicenter research combined cases of patients with recurrent glioblastoma and divided the clinical trials into two groups, those treated with bevacizumab and those treated with a variety of chemotherapy and never exposed to bevacizumab. The two cohorts were divided when applying a double Gaussian curve in ADC histograms and dichotomizing the ADC classifiers with a threshold set at ADC ~1.200 10^{-6} mm^2/s. In cases with mean values below threshold (μ<1.2) the odds for treatment response in anti-VEGF therapy were reduced, while both shorter progression-free survival and overall survival were detected compared to the other group of patients [20]. In other words, in cases of recurrent glioblastoma, pre-treatment ADC histogram analysis is a proven predictive imaging biomarker for anti-VEGF treatment in second-line therapy, but not chemotherapy. Low ADC values might be the result of either increased hypoxia or hypercellular tumor and when going beyond this knowledge, this could be the reason why a tumor with these characteristics shows resistance in anti-VEGF treatment. On the other hand, there are no biological data to support or reject this suggestion. The same group of scientists revealed that this threshold value of ADC, but with reverse use, enables patients' stratification of newly diagnosed GBM and serves as a predictive biomarker, too [33].

Epidemiologically and despite their specificities and significance, GBM and all primary brain cancers in general are less frequent than secondary / metastatic brain cancers. This statement further directs research towards metastasis into brain parenchyma and its similarities and alterations compared to GBM and recurrent GBM. A metastatic cancer is defined by the certain characteristics of its precursor lesion which, in the case of brain, is often located either in lung or kidney or breast. In cases of metastatic tumors, diffusion-based MRI techniques consider to be of high diagnostic value in distinguishing between GBM and metastatic lesions. To this respect, empirical observation of T2 and DWI images stand out GBM with infiltrative peritumoral edema and necrotic areas from metastatic lesions that are surrounded by a vasogenic peritumoral edema [8]. Furthermore, an interesting observation is that following a ROC curve ADC histogram analysis, a cutoff in peritumoral ADC value of ~1.300 10^{-6} mm^2/s for distinguishing between GBM and metastasis was revealed [34].

Considering the adjacent ADC values of 1.2-1.3 10^{-6} mm^2/s of primary, recurrent and metastatic brain tumors, above which patients seem to respond in bevacizumab, a main question that rises is whether these results could be correlated to HIF/VEGF levels and the extend of activation of HIF/VEGF-dependent signaling pathways. Also, given the fact of the similar response in bevacizumab treatment, an interesting study would also be the possible correlation through image analysis or in molecular level between recurrent and metastatic brain tumors, which although share similar topological area, they are of different cell origin.

In an attempt to answer the questions above in terms of biology, there was a supplementary work using the two cohorts of patients proposed by the previous study for cases with recurrent GBM subsequently treated with bevacizumab. In other words, in order to investigate if the poorer prognosis for patients with high-ADC tumors compared to those with low is associated with differential gene expression levels. For this reason, the two groups were divided according to pre-surgical scans and ADC values and after surgery, fresh frozen tumor samples were treated appropriately for microarray analysis and immunochemical staining. Gene-expression analysis show 13 significant genes which were over expressed in different ADC groups. Among the significant genes, 6 of them were either isoforms of collagen or collagen-binding proteins, all related to ECM. When gene expression was performed individually to test if there is any correlation with survival, only increased levels of decorin, a collagen-binding protein, was associated with increased risk of death, but not VEGF-A. Despite the fact that there was a significant ECM gene expression, data from immunohistochemical staining do not appear to correlate, mostly because of GBM's regional variation which do not allow representative sampling or measures of the tumor as a whole. In addition, the dimension of time could also contribute in the results, since VEGF levels seem to be depended on grade, size and as mentioned before, HIF-1a levels. This survey shows that high-ADC tumors overexpress genes of ECM, something that could be related to the GBM's invasive phenotype [21, 35].

Within the context of this postgraduate thesis, MRI methodology was integrated in:
1. a feasibility study, where pharmacokinetic parameters are derived from DCE-MRI using Toft's model and are used in order to feed **a glioma model** in terms of density of endothelial cells (vasculature) and helping in image areas of interest discrimination, under a set of assumptions
and 2. an *in silico* tracer kinetics study, where estimations of the transfer and disposition of GBCAs are made within a simulated brain tumor lesion (BTL) using PBPK modeling in order to evaluate the impact of vasculature.

PART I

A proposed paradigm shift in initializing cancer predictive models with DCE-MRI based PK parameters: A feasibility study

The extreme invasive and neoplastic growth of GBM has emerged the necessity to comprehend the mechanism of glioma growth, by using mathematical models. A number of different mathematical models have been proposed allowing description of tumor growth and invasion at different spatiotemporal scales [36, 37]. Among them, discrete mathematical models describe tumor cells as individual entities and study how their micro-interactions affect tumor behavior and morphology [38], while continuum approaches are better to describe tumors at tissue level assuming that tumor cells can be represented by densities or volume fractions [39-44]. Nevertheless, the incorporation of patient-specific, non-invasive imaging data to the existing mathematical approaches is of great importance for clinical practice, which is evident by the growing interest towards this direction [25, 45].
MRI is used for the estimation of tumor size, borders and vasculature. DCE-MRI is a technique where MRI sequences are obtained before, during and after the intravenous administration of a low-molecular-weight Gd chelate contrast agent. DCE-MRI data can later be processed using Toft's Model (TM) [46] in order to evaluate PK parameters that are able to quantify the differential leakage during the pass of the tracer's bolus in the tumor compartment of the model. DCE-MRI is frequently applied in brain oncology because of the prominence of vasculature that characterizes these tumors. This work focuses on the

feasibility of translating such anatomical information and functional imaging biomarkers into tumor characteristics in order to set the initial state of glioma growth models with perspectives on clinical outcome.
Several approaches attempting to decode cancer physiology through imaging biomarkers and use them towards initializing computational models with clinical data have been proposed. Swanson *et al.* [47] utilized two pre-treatment time points of Gd-enhanced T1-weighted (T1-Gd) and T2-weighted (T2) volume data to derive the microscopic tumor growth parameters of invasion and proliferation. Ellingson *et al.* [48] proposed a method of using serial diffusion-weighted MR (DW-MRI) images in order to estimate the same microscopic parameters. Szeto *et al.* [49, 50] combined MRI and positron emission tomography (PET) images from GBM cases to show that tumor aggressiveness estimated by a reaction-diffusion equation and MRI data is correlated with hypoxic burden visible on FMISO-PET. Recently Yankeelov *et al.* [24, 25] emphasized the importance of having a direct relevance to clinical outcome using both diffusion and perfusion MRI in order to parameterize a logistic growth model and predict chemotherapy effect and cellularity in breast cancer. Specifically, they used serial ADC measurements to estimate the tumor cell population and approximate the proliferation rate of tumor cells. Extended TM (ETM) was used in their work in order to incorporate PK parameters (v_e and v_p) into the estimation of tumor cell number, but not vascularity. However, in the latter study, a simple tumor growth model was used limited to the phenomena taken into account, while mounted on chemotherapy treatment of a rather more homogeneous type of cancer than GBM.

In this part, we focus on the feasibility of translating anatomical information and functional imaging biomarkers derived from DCE-MRI into tumor characteristics. Specifically, we suggest a method of using DCE-MRI in order to initialize an extended mathematical model proposed by Swanson *et al.* [51, 52] that describes the spatiotemporal evolution of tumor cells and their microenvironment. The model incorporates three types of cell populations (normoxic, hypoxic and necrotic), endothelial cells (building vasculature), angiogenic factors and oxygen concentration. The interactions among the different species are described using a system of coupled partial differential equations. DCE-MRI is used for extracting pharmacokinetic information and particularly K^{trans}, which is then used for 1. guiding tumor's compartments (viable cells and necrosis) selection within the region of interest (ROI) and 2. setting up the initial map of vasculature [52, 53]. To our knowledge, this is the first attempt of a glioma model initialization and validation based on the K^{trans} map. The methodology proposed is subsequently applied to a real clinical case. The simulated tumor vasculature is correlated to the real tumor and the effect of certain model parameters is also examined.

In the **following lines, the procedure followed is described regarding the model parameterization and the input data, as well as the assumptions made and patient information.**

MODEL ANGIOGENESIS, OXYGENATION AND DIVERSE CELL POPULATIONS

Cancer cells in solid tumors form a mass with augmented metabolic needs due to constant vigorous changes. As the solid tumor develops, it must generate its own blood supply due to insufficient diffusion of nutrients and oxygen from pre-existing vasculature. Intra-tumoral hypoxia is considered to be the main driving force of induced angiogenesis within the tumor in agreement with Folkman's assertion [54]. Hypoxia-inducible factor (HIF-1α) is a transcription factor that promotes ischemia-driven angiogenesis through the induction of differential expression of the VEGF. VEGF appears to be a key-molecule for both the pro-angiogenic events and the survival of newly formed vessels [1]. At a cellular / tissue level, the series of events is a multi-step repeatable process. In brief, first, the pre-existing neighboring vessels

stretch and expand towards tumor as a response to the pro-angiogenic factors released by cancer cells. The new endothelial cells migrate in a concrete way while degrading concurrently the extracellular matrix (ECM) and eventually form tube structures [35, 55, 56]. However, the mechanisms of angiogenesis in tumors fail to promote mature vascular networks and lead in formation of abnormal, leaky, tortuous and/or shunt vessels [57], which fail to restore oxygen supply in hypoxic regions which further induces HIF expression and a perpetual cycle of events from hypoxia and HIF-1α expression to VEGF, angiogenesis and tumor growth.

The mathematical model used in this work [51, 52], incorporates the angiogenic cascade and oxygen supply as interact with tumor cell populations. Depending on oxygen availability, tumor cells can be normoxic, hypoxic or necrotic. Thus, the different components of the model are the concentrations of normoxic cells (c), hypoxic cells (h), necrotic cells (n), angiogenic factors (a), endothelial cells building vasculature (v) and oxygen (o). The interacting species are described using a system of coupled, partial differential equations of reaction-diffusion type (1-6).

More specifically, the model assumes that normoxic cells (1) diffuse at rate D, proliferate at rate ρ and covert to hypoxic and necrotic cells at rates β and a_n, respectively. Hypoxic cells (2) are assumed for simplicity to diffuse at the same rate D, they do not proliferate but, can convert to normoxic cells at rate γ when oxygen becomes available. Necrotic cells (3) derive from normoxic, hypoxic and endothelial cells that die at a rate a_n when in contact with necrosis as well as from hypoxic cells that turn to necrotic when oxygen is insufficient. Continuing as described in [51, 52], endothelial cells structuring vasculature (4), migrate with a diffusion rate D_v, increase their population at a rate a_v and die at a rate a_n. Angiogenic factors (5) diffuse with a diffusion rate D_a, are produced by normoxic and hypoxic cells at rates δ_c and δ_h, respectively, consumed by endothelial cells at rate $q\,a_v$, decay at a rate λ and are washed out by the vessels at a rate ω. Finally, oxygen diffuses at rate Do, decays at rate a_o, is produced by vasculature with a rate β_o and is consumed by normoxic and hypoxic cells at rates γ_{oc} and γ_{oh}, respectively. For all above equations, T is a capacity variable defined as $T = (c + h + v + n)/k$, where k corresponds to the maximum capacity of a voxel, i.e. the maximum number of cells it can host.

$$\frac{\partial c}{\partial t} = \nabla \cdot (D(1-T)\nabla c) + \rho c(1-T) + \gamma h o - \beta c(1-o) - a_n n c \quad (1)$$

$$\frac{\partial h}{\partial t} = \nabla \cdot (D(1-T)\nabla h) - \gamma h o + \beta c(1-o) - (a_h(1-o) + a_n n)h \quad (2)$$

$$\frac{\partial n}{\partial t} = a_h h(1-o) + a_n n(c+h+v) \quad (3)$$

$$\frac{\partial v}{\partial t} = \nabla \cdot (D_v(1-T)\nabla v) + a_v v(1-T) - a_n n v \quad (4)$$

$$\frac{\partial a}{\partial t} = \nabla \cdot (D_a \nabla a) + \delta_c c + \delta_h h - q a_v v(1-T) - \omega a v - \lambda a \quad (5)$$

$$\frac{\partial o}{\partial t} = \nabla \cdot (D_o \nabla o) - a_o o + \beta_o v - \gamma_{oc} c - \gamma_{oh} h \quad (6)$$

The spatiotemporal solution of the system is approximated by applying the Alternative Direction Implicit method of finite differences in three spatial dimensions [58, 59].

EXTRACTING PK PARAMETERS FROM DCE-MRI

PWI-MRI may characterize the rate delivery of nutrients via blood into brain tissue parenchyma. The maps that are constructed through the analysis of such data reveals microvasculature information, which can be correlated to the levels of angiogenesis and the grade of the tumor.

DCE-MRI is performed by acquiring T1-weighted images before, during and after the intravenous injection of a low-molecular-weight gadolinium chelate which enters to the blood circulation and is deposited to the tissue without entering the cells. Due to the disruption of the blood brain barrier (BBB), tumor sites

show a faster swift and acute development than healthy background tissue, followed by de-amplification after repletion of the available space [27]. The boosted infiltration and vascularization of tumor lesions leads to enhanced permeability of contrast agents in blood vessels supplying the tumor which results in corresponding 'bright' image regions in the post contrast phase during image acquisition. Afterwards, the Gd tracer evacuates the tissue with re-entrance to the blood vessels.

The concentration of the contrast agent along with other parameters such as the transport rate constants are measured when passing through the vessels to the extracellular space and vice versa. DCE-MRI is used for the calculation of the vascular permeability constants through pharmacokinetic models and is a useful tool for characterizing tumor blood vessels and different compartments of the affected tissue. In other words, Gd concentration needs to be translated in a PK parameter in order to be utilizable for our approximation.

TM [46] is often used to quantify the permeability of the vessels by the measurement of K^{trans} (min^{-1}), the transfer constant between blood plasma and extravascular-extracellular space (EES) which is indicative of the volume of blood that flows out of the vessels; u_e, the volume of EES per unit volume of tissue that represents the volume of blood which flows out of the vessels, and k_{ep}, the rate constant between EES and blood plasma (min^{-1}). These three parameters are related as follows:

$$k_{ep} = \frac{K^{trans}}{u_e}. \quad (7)$$

In TM it is assumed that as soon as contrast agent is injected into the blood stream it is able to pass across the blood vessel endothelium to the tissue's extracellular space at a rate that is proportional to the difference in concentration between plasma and tissue:

$$\frac{dC_t}{dt} = K^{trans}\left(C_p - \frac{C_t}{u_e}\right) \quad (8)$$

where C_t is the concentration of contrast agent in the tissue and C_p is the concentration in the plasma (arterial input function - AIF).

The solution of Equation [8] is:

$$C_t(t) \approx u_e \cdot C_e = C_p * (K^{trans} \cdot e^{-t \cdot K^{trans}/u_e}) \quad (9)$$

with given C_t (from converting signal intensities (SI) of DCE-MRI data to concentration) and C_p (measurement of AIF either from data or assuming a theoretical value), we can solve the parameter estimation problem from Equation [60] in order to fit the K^{trans} and u_e values. The system to be solved represented by Equation [60] is depicted in the next figure with typical types of the curves.

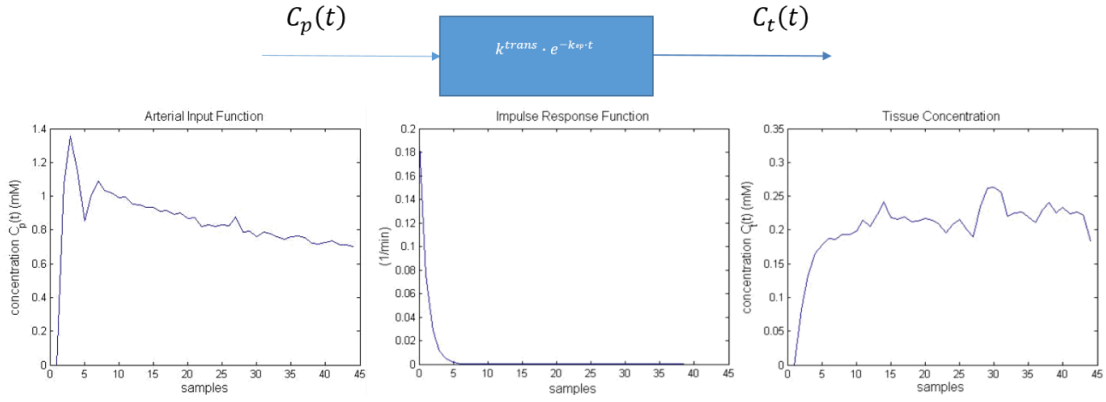

Figure 3_ ***(Example)*** *The single input and single output representation of TM. The model assumes as input the AIF (same for all voxels) and output the converted SI to tissue concentration C_t of each voxel. Thus, the impulse response function should be estimated for each voxel, which is described by*

THE ROLE OF PK IN SETTING UP THE INITIAL STATE OF GBM MODEL

The main focus of this work is to use the DCE-MRI PK parameters, which reflect the physiology of the tumor, in a way that they could give a more realistic estimation of the model's initial parameters and set their default bounds. The precise set of values is patient-specific since they depend on a DCE-MR image referring to a particular brain tumor.

Based on DCE-MRI we can estimate the vascular permeability constants for an agent driven effectively through the blood vessels. Moreover, though Gd passes through the endothelium of the blood vessels, it cannot pass through the cancer cells and thus, it remains in the EES until its resorption. In DCE-MRI, there is no linear relationship between the Gd concentration and the signal intensity of the tissue. In our approximation, the transfer constant, K^{trans}, is used, which represents a measure of trans-endothelial transport of Gd from the vessels to the tumor interstitium [61]. K^{trans} is assumed to be indicative of the tumor's morphological features in a twofold way: **1.** the image areas of interest, and **2.** the micro-circulation.

SETTING UP THE REGION OF INTEREST AND NECROSIS

The first to be determined is the location and the space occupied by the tumor or alternatively, the region of interest (ROI). Comparing the enhancement showed in a DCE-MR image by a GBM tumor mass to the neighboring healthy tissue, GBM appears to be more intense due to the loss of the BBB within the majority of the tumor blood vessels and the subsequent intensified Gd efflux from the vasculature. Note that in the data used in our model implementation, acquisition time of DCE-MR images was around 5 minutes in total. Given that Gd clearance can be fully attributed to renal excretion, the fact that Gd does not enter in the cells [61] and in combination with such a short time of scanning, the visible Gd concentration can be assigned only to direct Gd exchange to and from the blood circulation where blood vessels exist (and not to passive Gd diffusion).

Additionally, as already mentioned, the infiltrative nature of the edema of the GBM is confined in the peritumoral region with a small percentage of vasculature. Thus, there is limited, if any, concentration of Gd tracer in the area surrounding the tumor and no enhancement in the K^{trans} map [8, 9]. Despite the fact that the intense of the infiltrative edema should approximate the intensity of the cerebrospinal fluid (CSF), this is not that clear due to the dark background of the either above or below non-affected tissue (figure 4) within a slice. In this way, we can define the ROI from PK analysis in a DCE-MR image as the enhanced area of the GBM plus the interior necrotic core [50].

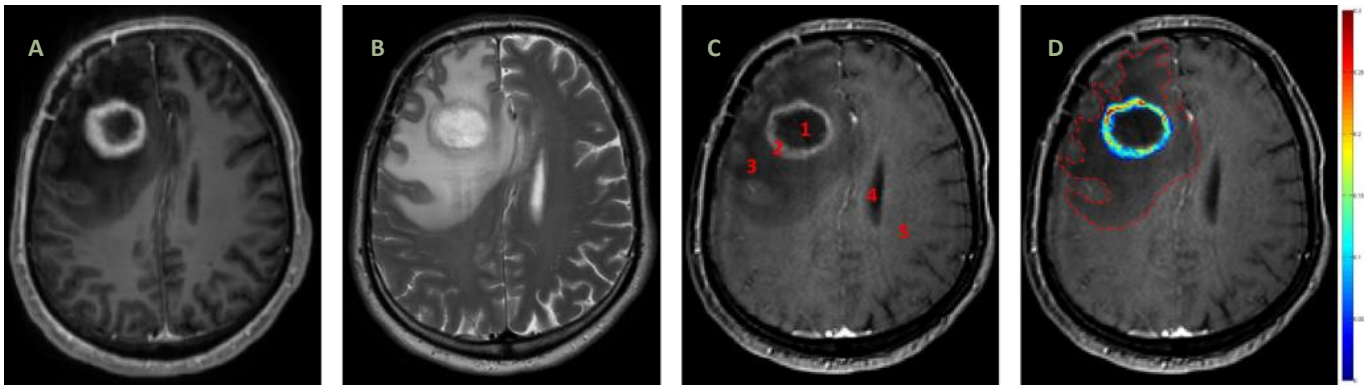

Figure 4_ *Clarification of discrete regions with delineation based on signal intensity in histologically proven GBM tumor. Ventral surface of axial sections through dorsal portions of corpus callosum.* ***A:*** *Post-contrast T1-weighted MR image with higher resolution;* ***B:*** *T2-weighted MR image with water and fluid (i.e. edema) appearing bright;* ***C:*** *DCE-MR image where different regions are noted, 1. non-enhancing necrotic core, 2. tumor mass (normoxic and hypoxic cells) seen as a bright, ring-shaped tumor in the right frontal lobe, 3. hypointense peritumoral edematous infiltrating area, 4. lateral ventricle with cerebrospinal fluid, and 5. normal white matter (control);* ***D:*** *The same DCE-MR image with superimposed the Ktrans color-map and with the dotted line showing the borders of the edema surrounding the tumor and extending to both the medio-lateral and the antero-posterior axes.*

Moreover, K^{trans} is indicative of necrosis [50]. The necrotic core of the brain tumor is not expected to maintain any vessels and thus, there is lack of enhancement in the MR signal intensity (SI) that is, the value of K^{trans} is zero. In order to be more precise in the determination of the fraction of the ischemic necrosis, the chosen area was set right inside after the nulls of K^{trans} spotted in the K^{trans} map. In other words, there is a sequence of areas with interchanged, attenuating or not, brightness. This observation was verified by a radiologist in each case.

SETTING UP THE INITIAL MAP OF VASCULATURE

Angiogenetic mechanisms of vascularization in GBMs result in newly formed neoplastic vessels which are leaky, tortuous and abnormal with irregularly increased permeability, larger pores and fluid retention problems [57]. The immatureness of the newly formed blood vessels may also explain the tendency of the BBB permeability. Furthermore, Gd tracers on the contrary to oxygen (O_2), have a much higher molecular weight which makes obvious that there is a need for generally more permeable vessels in order to come out. This is what forces the Gd to exit from the vasculature and diffuse within the tumor interstitium. We assume:

1. high permeability for any vessel inside the tumor mass and
2. within the tumor regions that are in the same level of oxygenation, these vessels are homogeneously allocated.

Because of the existence of many vessels, the average vessel within a voxel is expected to satisfy these assumptions. Thus, since TM itself provides no particular information about the physiology of the vessels with any impact on steric effects, i.e. size of pores or diameter, there comes the emerging property that the higher the Gd concentration, the more the vessels in number. In this way, the higher the K^{trans} value, the higher the percentage of the vessels.

By taking this second assumption in the model, there is a division of the tumor volume in classes with different levels of vasculature and consequently more or less effective oxygenation. What is worth to be noted is that K^{trans} is a quantitative measure and voxel-specific, such that both the temporal and the spatial resolution remain high.

INFORMATION ABOUT THE PATIENT

The patient is chosen to be either not-responding or untreated because the primary aim is to focus on free tumor-growth patterns for method validation. However, it has to be clarified that it is hard to find patients either without resection or untreated for the entire duration of the disease. The dataset preferred is from a patient with two time points of DCE-MR images; the diagnostic and the follow-up clinical examinations with 39 days apart.

The clinical case used is taken from a patient with recurrent GBM, classified as stable disease using the Response Assessment in Neuro-Oncology (RANO) criteria, currently the clinical standard in the radiological follow-up of high grade glioma patients (Table 4 in APPENDIX). The data were taken from an imaging study approved by the local ethics committee of the University Hospitals Leuven, Leuven, Belgium. The DCE-MRI were acquired with a 3.0T scanner (Achieva, Philips Medical Systems) using an é-channel head coil for reception and the body coil for transmission.

The presence of new lesions and the generalized tumor volume progression make this case appropriate for our study. The central necrotic lesions are located in the right frontal lobe. There is extensive edema, causing mass effect on the frontal horn of the right lateral ventricle. The treatment that he followed and responded to is immunotherapy and has no clear impact on the factors taken into account in this work. Apart from immunotherapy, radiation was used but not in the first two time points of the model execution. This is why we avoided using the second follow up for a second evaluation of our method. One

more thing to be declared is that there is a mark from biopsy, but there is no effect of hemorrhage in the tissue.

STEPPING FROM REGION OF INTEREST TO DISCRETE TUMOR AREAS

As already mentioned, based on K^{trans} intensity map, the image area of necrosis ($K^{trans} = 0$) and the tumor's area with viable cell populations ($K^{trans} \neq 0$) are defined within the ROI. Thus, although necrotic cells are concentrated in areas with no K^{trans}, hypoxic and proliferative cells are not discriminable with pharmacokinetic parameters. The next procedure refers to the shape determination of the necrotic area as well as to an oversimplified discrimination between normoxic and hypoxic areas. In any case, necrosis is in the center, hypoxia is to tumor's interior and normoxia to the periphery.

As shown in figure 5, the interior core of the K^{trans} is associated with areas of no vasculature. The areas that are nearly adjacent to the vascularized ring (intersection of the two areas) can be assumed to get marginally oxygenated and not necrotic. Therefore, in order to define the necrotic area, we erode away the area where $K^{trans} = 0$ until it shrinks about 10%. In order to discriminate hypoxic and normoxic regions, we assume that proliferative cells must have their highest density towards the periphery [62], while the hypoxic area must be considerably wider than the normoxic ring. Thus, in order to leave a thin proliferation ring around the tumor surface, we similarly erode away the area where $K^{trans} \neq 0$ testing several different volume reductions. The erosions were made using a 3x3 morphological operator which differs according to the desirable shrinkage. For example, for a 10% shrinkage of the eroded area, the mask [0 1 0; 1 1 1; 0 1 0] would be appropriate. Either consecutive erosions using the same mask or a different mask can be used. In our trials, we used different masks in order to decide the final extends of areas. The operator forms gradients instead of sharp edges since there is a smooth transition between the areas and cell populations that switch in model's equations.

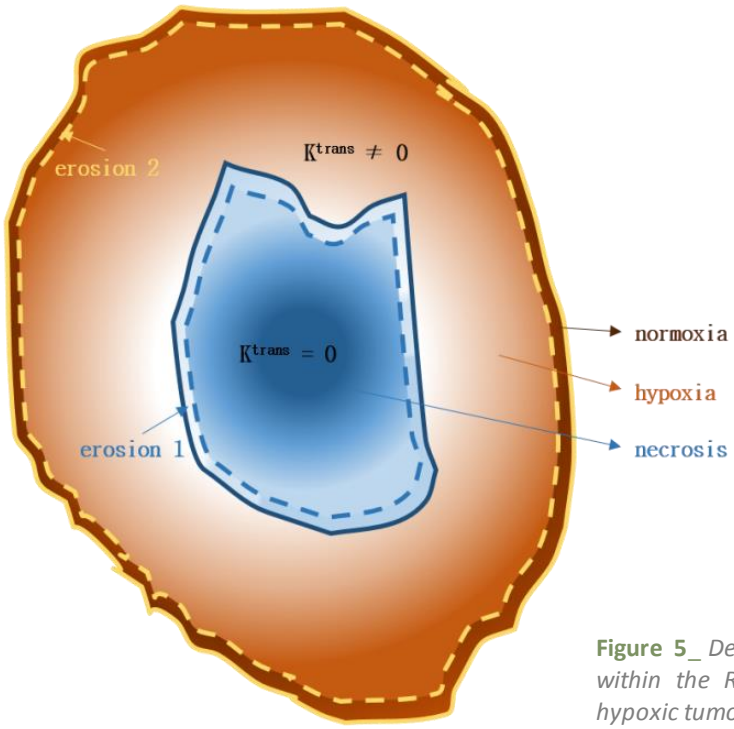

Figure 5_ *Depiction of shape formation of the tumor areas within the ROI. Dashed lines represent the erosions. The hypoxic tumor area extends between the two dashed lines.*

Before feeding the model with parameters, the system of equations (1-6) was non-dimensionalized according to previous studies [51, 52]. The length scale was set to $L = 27{,}08\text{cm}$ and the time scale was set to $\tau = 8h$. We rescaled cell densities with the maximum cell density, $k = 10^8 \frac{cells}{cm^3}$ and angiogenic factors with $a_{max} = 5.75\ 10^{-4} \frac{mmol}{cm^3}$. The set of all the parameters used in our model are depicted in Table 2.

Two time points of DCE-MR images from a GBM patient are avaialble. The first image was used for model initialization, whereas the follow-up for validation. The original dataset consists of 37 192x192-pixel DCE-MRI slices. The MRI images and the respective K^{trans} maps have been interpolated to a 96x96x96-voxel volume.

Figure 6 shows an exemplar slice of the initial vasculature as derived from the K^{trans} map after normalization to $v_{0,max} = 10^{-2}$ [52]. In the absence of any additional information and considering that GBMs are highly diffusive brain tumors, we set the maximum initial concentrations of each normoxic (c_0), hypoxic (h_0) and necrotic (n_0) subpopulations to 1/3 of the maximum voxel capacity. However, we must stress out that other values were also tested (2/3 and 1, data not shown) and proven to be inappropriate because the simulated tumor mass appeared to be homogeneous and highly rigid, contrary to the expected heterogeneity and diffusiveness of a real GBM tumor. Figure 6 shows the initial normoxic, hypoxic and necrotic subpopulations. Note that there are areas that overlap between the three regions and that peak densities are located in the periphery, the interior and the center for normoxia, hypoxia and necrosis, respectively. Furthermore, erosion shrinks the periphery of necrosis by 1mm, which can be assumed a valid maximum distance for oxygen to be transferred [63] from the $K^{trans} \neq 0$ to the $K^{trans} = 0$ region. The ring of proliferative area in figure 6 has a mean width of 1mm [62, 64].

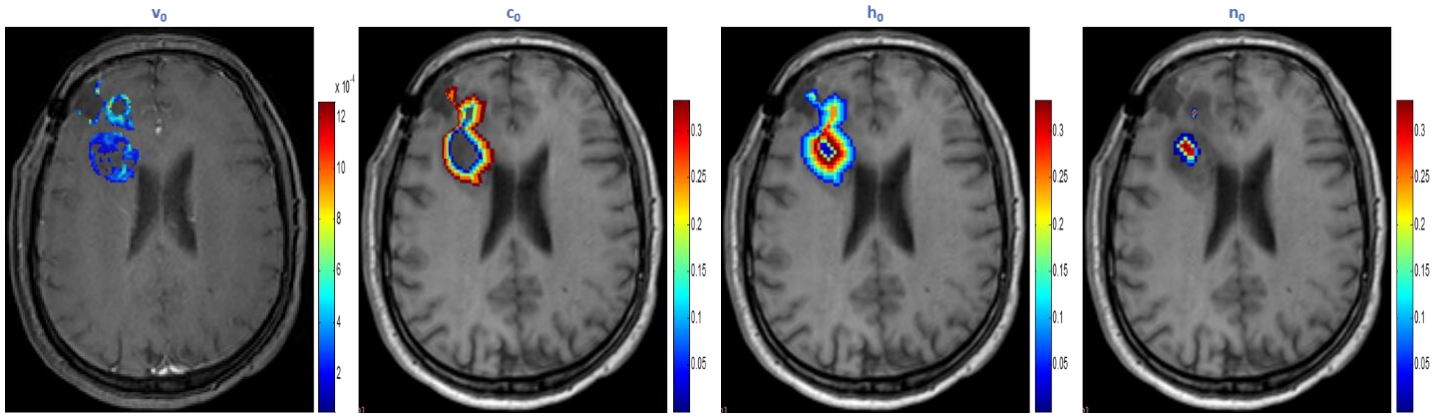

Figure 6_ *Initial concentration of vasculature (v_0), normoxic (c_0), hypoxic (h_0) and necrotic (n_0) cells projected on the 57th slice of the initial state, after interpolation.*

K^{trans} is not informative regarding levels of angiogenic factors. Thus, negligible value of the angiogenic factors was initially chosen (a_0=0). Indeed, we will show in the following sections that different initial values of angiogenic factors have minimal effect on tumor growth. For simplicity, we also assumed that initially the oxygen concentration was set to its maximum saturation value; that is 1. It is important to mention that at the moment studied, the tumor has generated its own blood supply and is characterized by augmented metabolism. Thus, the initial vasculature is expected to play a critical role in tumor evolution, while the need for consumption will quickly configure oxygen dynamics, which will further determine the distributions of normoxic, hypoxic and necrotic subpopulations and angiogenic factors.

Table 2 MODEL PARAMETERS FOR SIMULATION AND THEIR NON-DIMENSIONALIZED VERSIONS [53]

Parameter	Value	Non-dimensionalized	Parameter	Value	Non-dimensionalized
$\boldsymbol{\rho}$	$0.0087\left(\frac{1}{day}\right)$	$\tau\rho$	$\boldsymbol{\beta}$	$\frac{\rho}{10}\left(\frac{1}{day}\right)$	$8.7\ 10^{-4}$
$\boldsymbol{\gamma}$	$0.05\left(\frac{1}{day}\right)$	$\tau\gamma$	$\boldsymbol{D}$	$3.6\cdot 10^{-8}\left(\frac{cm^2}{s}\right)$	$\frac{\tau}{L^2}D$
$\boldsymbol{a_n}$	$\frac{ln2}{50}\left(\frac{1}{day}\right)$	$\frac{ln2}{150}$	$\boldsymbol{D_v}$	$3.6\cdot 10^{-9}\left(\frac{cm^2}{s}\right)$	$\frac{\tau}{L^2}D_v$
$\boldsymbol{a_h}$	$\frac{\rho}{20}\left(\frac{1}{day}\right)$	$4.35\ 10^{-4}$	$\boldsymbol{D_a}$	$10^{-3}\left(\frac{cm^2}{s}\right)$	$\frac{\tau}{L^2}D_a$
$\boldsymbol{\mu}$	$\frac{ln2}{15}\left(\frac{1}{day}\right)$	$\tau\mu$	$\boldsymbol{K_m}$	$5.75\ 10^{-7}\left(\frac{mmol}{cm^3}\right)$	$\frac{K_m}{a_{max}}$
$\boldsymbol{\delta_c}$	$7.59\ 10^{-16}\left(\frac{mmol}{cell\ day}\right)$	$\frac{\tau k}{a_{max}}\delta_c$	$\boldsymbol{\lambda}$	$\frac{ln2}{64}\left(\frac{1}{min}\right)$	$\tau\lambda$
$\boldsymbol{\delta_h}$	$1.43\ 10^{-12}\left(\frac{mmol}{cell\ day}\right)$	$\frac{\tau k}{a_{max}}\delta_h$	$\boldsymbol{\omega}$	$1.43\ 10^{-12}\left(\frac{1}{cell\ day}\right)$	$tk\omega$
$\boldsymbol{q}$	$10^5\left(\frac{mol}{cell}\right)$	$\frac{k}{a_{max}}q$	$\boldsymbol{D_o}$	$0.036\left(\frac{cm^2}{s}\right)$	$\frac{\tau}{L^2}D_o$
$\boldsymbol{a_o}$	$0.0013\left(\frac{1}{day}\right)$	τa_o	$\boldsymbol{\beta_o}$	$0.05\left(\frac{1}{day}\right)$	$\tau\beta_o$
$\boldsymbol{\gamma_{oc}}$	$3.125\left(\frac{1}{day}\right)$	$\tau\gamma_{oc}$	$\boldsymbol{\gamma_{oh}}$	$2\gamma_{oc}\left(\frac{1}{day}\right)$	$\tau\gamma_{oh}$

RESULTS

The simulation results after initializing vasculature and cell densities according to the described procedure are presented below. An exemplar slice of the original K^{trans} map of the follow-up examination, which was performed 39 days after the initial examination, is also presented in figure 7 for comparison. Within the frame of figure 7 are illustrated the spatial distributions of the predicted vasculature (v), normoxic (c), hypoxic (h) and necrotic cells (n) as well as the angiogenic factors (a) after 39 fictitious days of the same slice. The tumor increases in size, while hypoxic cells maintain the larger space within the tumor and hypoxia-driven angiogenic factors are homogeneously allocated inside this hypoxia-bounded area.

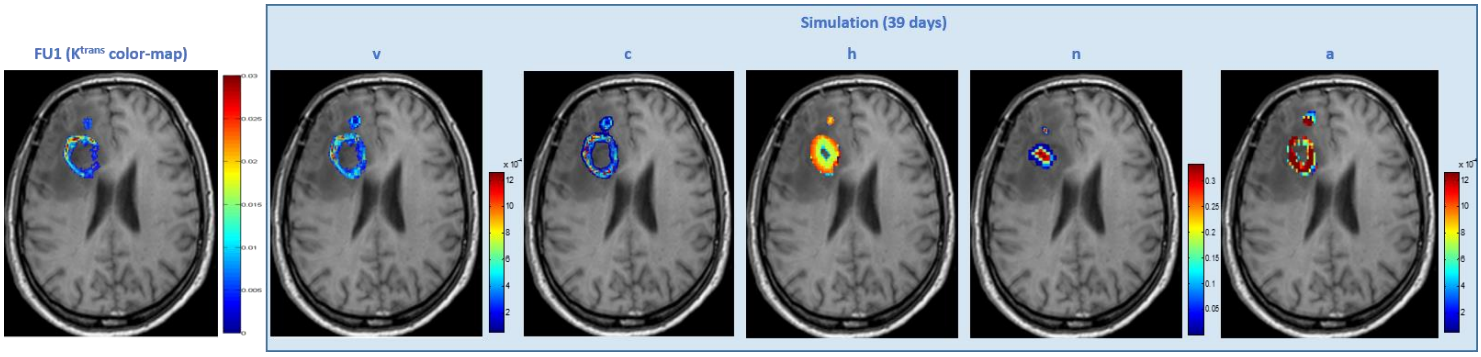

Figure 7_ ***Left:*** *57th slice with the K^{trans} map extracted from the real dataset of the FU1 session;* ***within the frame:*** *the simulated concentrations v, c, h, n, a of vasculature, normoxic cells, hypoxic cells, necrotic cells and angiogenic factors, respectively.*

Figure 8 shows the concentrations of the normoxic, hypoxic and necrotic subpopulations over time. The total tumor population consisting of the sum of normoxic, hypoxic and necrotic cells follows a Gompertzian-like growth where an initially fast growth is followed by a slowdown phase. The normoxic subpopulation slightly decreases over time until it almost stabilizes, while hypoxic cells initially increase fast and then slow down where a plateau is reached. Although slightly, necrosis also increases over time. As can be seen in figure 8, hypoxic cells dominate within the tumor indicating that oxygen supply is

insufficient for the increasing metabolic demands of tumor cells. All populations start from a non-zero value determined by the initialization process. The tumor continues processing after the 39 days.

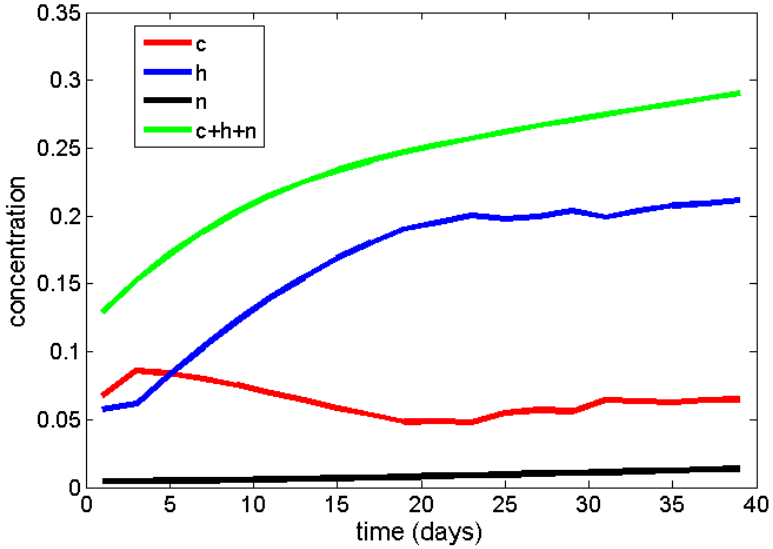

Figure 8_ *The growth curves of the simulated concentrations* $\boldsymbol{c}, \boldsymbol{h}, \boldsymbol{n}$ *and the entire tumor* $(\boldsymbol{c} + \boldsymbol{h} + \boldsymbol{n})$ *computed on the whole 3-dimensional grid. Vertical axis is the non-dimensionalized concentration and horizontal axis is time (days).*

Figure 9 presents the growth of vasculature (left) and angiogenic factors (right) in time. Inevitably, vasculature keeps increasing consistently to the tumor growth. These biological phenomena are causally related. As already discussed, hypoxia leads to the expression of (pro-) angiogenic factors like VEGF, which in turn promote angiogenesis and the formation of vasculature in hypoxic areas. Note that a few days after hypoxic cells start increasing (figure 9), both the levels of angiogenic factors and vasculature are rapidly multiplied (day 12 in figure 9). However, as hypoxic cells reach a plateau, the concentration of angiogenic factors is stabilized and vasculature keeps increasing.

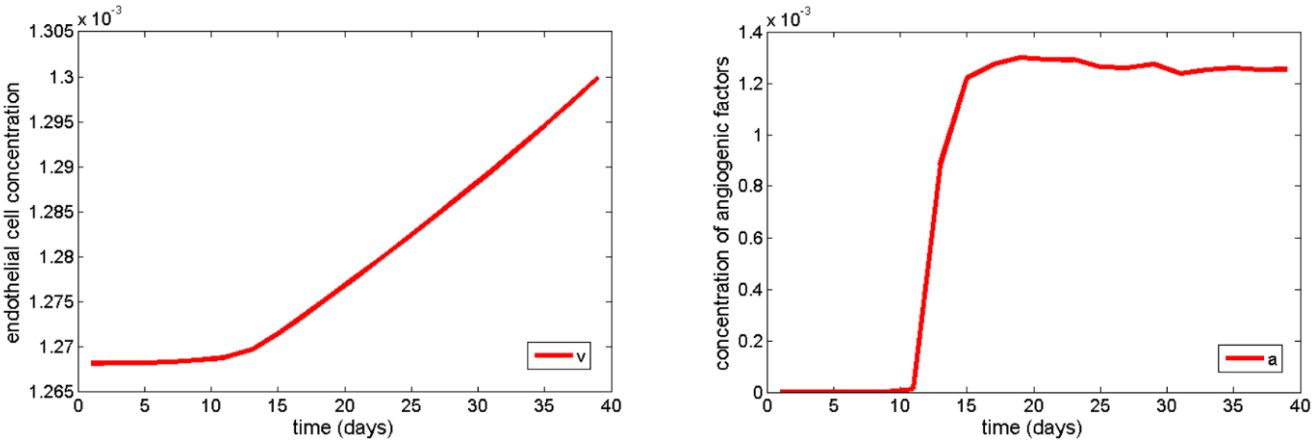

Figure 9_ *The growth curves of the simulated vasculature (**left**) and angiogenic factors (**right**) computed on the whole 3-dimensional grid. Vertical axis is the normalized concentration and horizontal axis is time (days).*

The goal of the present study is to demonstrate a way to incorporate DCE-MRI data into a mathematical model of glioma growth that takes into account the angiogenic cascade in order to predict GBM development. Specifically, DCE-MRI is used for extracting the pharmacokinetic parameter K^{trans}, which is then used for model initialization and validation. This is both originated and addressed to patients, targeting in clinically comparable outcome.

Regarding the results of the simulation, as shown in figure 7, there is an agreement in the pattern of vasculature density v (produced by model) and the K^{trans} map of the FU1 session. It is observed, that the three peaks and the density's pattern seen in FU1 are repeated in v, while the smaller anterior part of the tumor is remarkably shrunken in size, like in the real tumor (figure 7). However, the model's prediction as regards the medial extend of the tumor is slightly overestimated.

The transient limited shrinkage can be connected to initial high level of necrosis locally and/or unknown treatment efficacy, but eventually the tumor gradually spreads. This is noted in a second follow up dataset, not shown here (figure 18 in APPENDIX). Though this phenomenological shrinkage can be explained in terms of biology, there is no such information given to the model. Since the simulated tumor is approximately registered to the real one because of the interpolation procedure, we checked the slices above and below the one presented here and there is no separation between the two parts, while the anterior part also develops. In any case, it has to be clarified that it is a qualitative comparison on an arbitrary chosen 2D slice.

In the following, different values of critical modeling parameters are examined and quantitative metrics are used in order to better evaluate the outcome of our results.

EFFECT OF PARAMETERS

It is important to see how results differentiate with some basic model parameters. The first parameter studied was the diffusion coefficient, D, of tumor cells. Specifically, we explore how the simulated vasculature is affected when changing the diffusion rate of cells. Figure 10 shows the predicted spatial distribution of v for $0.1D$ and $10D$, where $D = 3.6\ 10^{-8}\ cm^2/s$ (Table 2) is within the range of relevant literature [51]. For comparison, Figure 10 also shows the original K^{trans} map of the follow-up examination as well as the predicted v for the original value of D. As expected the pattern of v for low D is highly saturated, as the inability of tumor cells to migrate fast increases their local densities and consequently their demands for new vasculature. On the other hand, higher values of D result in an increase in tumor size and produce a pattern where vasculature seems more extended and scattered than the original corresponding data of K^{trans}. A quantitative comparison has been also performed and presented in the next section.

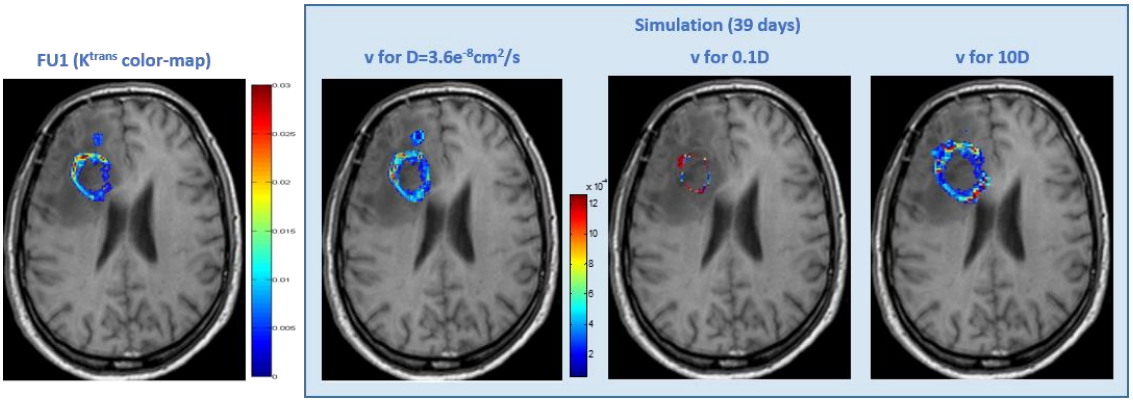

Figure 10_ *Effect of the different values for the diffusion coefficient, D, to the resulting vasculature.*

The next step is to study the effect of proliferation rate ρ to the results. Figure 11 shows how results differ for 0.1ρ and 10ρ, where $\rho = 0{,}0087\ 1/day$ (Table 2) complies with bibliography [65]. The pattern of v for high ρ (i.e. cells divide faster) shows a saturation of v, as increased cellular proliferation leads to increased tumor densities and metabolic demands that stimulate increase in vasculature. On the other hand, lower ρ produces a pattern where vasculature seems more dispersed. Different values for both D and ρ were also tested (data not shown), but none reflected better the real FU1 than the pair of values finally chosen.

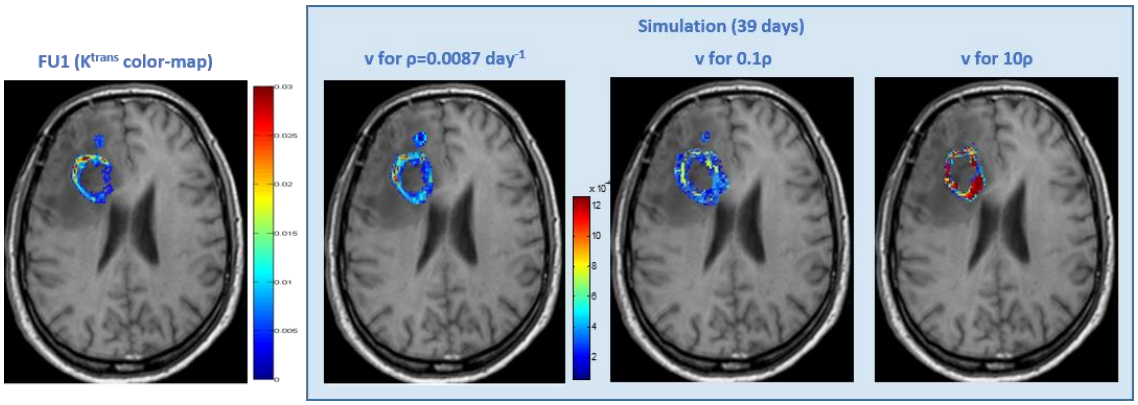

Figure 11_ *Effect of the different values for the proliferation rate, $\boldsymbol{\rho}$, to the resulting vasculature.*

As stated previously, the initial density of angiogenic factors a_0 was set to zero. Once again, this model parameter was checked for values other than zero and particularly, a_0 was alternatively set to the maximum value of 1. Initially, a steep drop by approximately three orders of magnitude of the angiogenic factors is observed as their consumption relative to their production is significantly higher (figure 12). However, as tumor evolves and hypoxia increases, an increase in the angiogenic factors is also observed similar to that of figure 9 (left). Interestingly, the resulting graphs of the three tumor populations and the overall tumor growth, as also the growth of endothelial cells in time appear to be almost the same as in figures 8 and 9 (left). This indicates that the choice of initial a does not substantially affect the model's outcome.

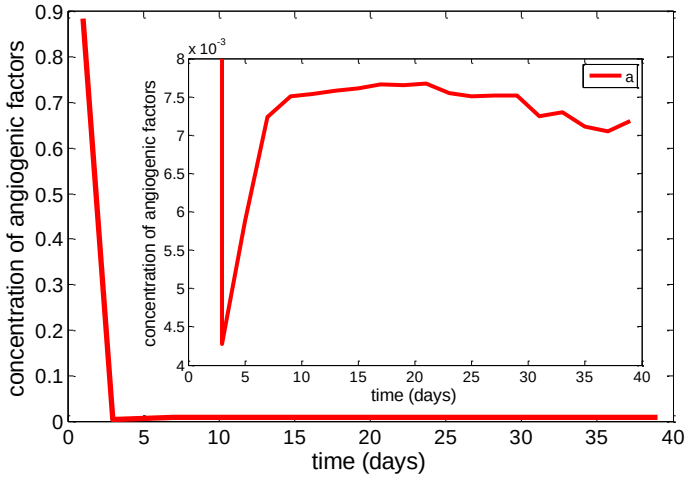

Figure 12_ *The growth curve of the simulated angiogenic factors for $\boldsymbol{a_0 = 1}$. A zoom into the phase after the steep drop (day 3) of the concentration of the angiogenic factors is also shown.*

METRICS FOR 3D SIZE COMPARISON

To get a better aspect of the results, it is important to make a quantitative evaluation of the agreement between the simulated tumor and the final tumor. For evaluation, we use a scheme that uses solid metrics and provides objective comparison. Therefore, if the final pattern of K^{trans} is used as golden ground truth for vasculature, then we can adopt the Jaccard (JC), Dice (DS) and Volume Similarity (VS) metrics for identifying similarity [39-44]. JC, DS and VS are defined as:

$$\mathbf{JC=TP/\ (FP+TP+FN)}$$
$$\mathbf{DS=2TP/\ (FP+2TP+FN)}$$
$$\mathbf{VS=1-|FP-FN|/(FP+2TP+FN)}$$

TP (True Positive) is the number of tumor voxels belonging to both the ground truth and simulated result, FP (False Positive) is the number of tumor voxels belonging to simulated result, but not found in ground truth and FN (False Negative) is the number of tumor voxels belonging to ground truth but not found in the simulated tumor.

For eliminating noise and artifacts we set the detection threshold as 10% of maximum value for both ground truth and test datasets. The following graph presents the resulting metrics for different cases of parameters. Metrics regarding the uniform initialization of vasculature (uniform v) is noted, since it is commonly used in absence of relevant information (also proposed by [52], figure 19 in APPENDIX). The scores for uniform vasculature are remarkably lower than the rest cases. Additionally, multiple erosions with different morphological operators were tried regarding the configuration of the area of the proliferative ring. However, this is not the case for the erosion of the necrotic core since the chosen erosion is representative of the population of cells changing between necrotic and hypoxic areas. Normoxic area diameter varied from 0mm (no erosion) to ~ 10mm (minimum hypoxia). As it can be seen from the graph, all metrics' scores are inversely proportional to the normoxic area expansion (erosions 1-5mm show minimal differences). Alternatively, the less the assumed hypoxic region by erosion, the more inaccurate the model predictions become. According to our trials, the erosion of 1mm appears to be the most appropriate. The parameters used in our approximation were selected to produce the highest scores for all three evaluation metrics. All the evaluation metrics results are shown in detail below in table 5 (APPENDIX).

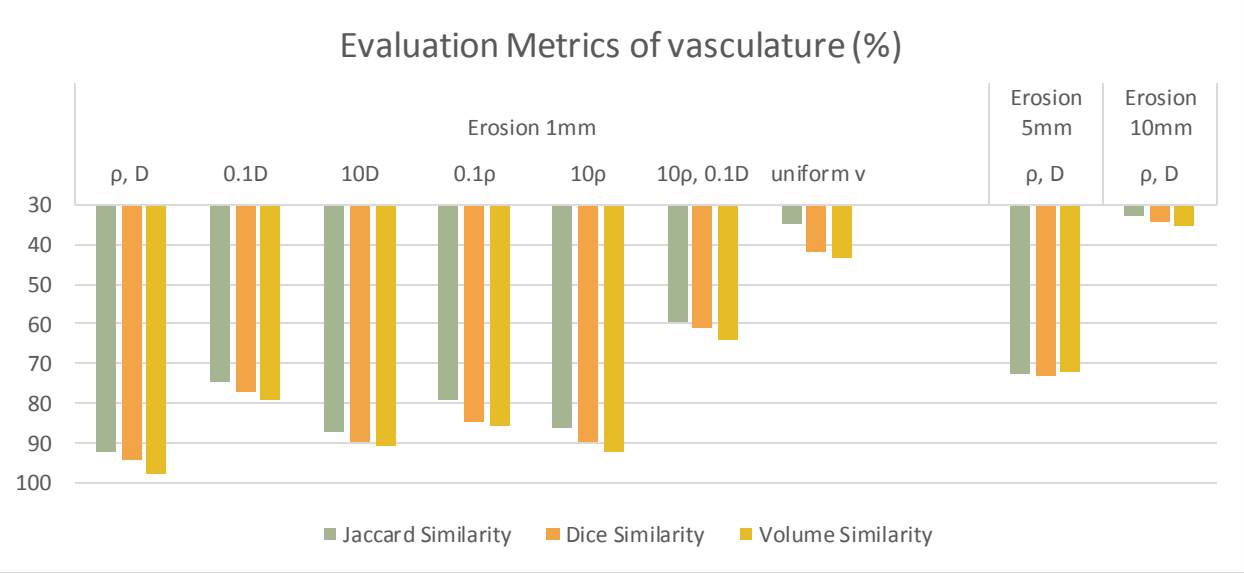

The evaluation metrics enable comparing the vasculature of the simulated tumor and the K^{trans} of the real FU1 tumor, concerning their volumes. A cross-correlation analysis should be made in order to further evaluate their internal transdifferentions beyond size.

The K^{trans} map of the FU1 image and the associated vasculature profile of the *in silico* approximation are shown below in figure 13. Higher values of either K^{trans} or vasculature density are expected at lower frequencies within a tumor mass. The calculated correlation coefficient is $R = 0.8861$, after truncating all zero values for K^{trans} and v. Taken all together the evaluation results show that the two tumors are strongly correlated both in means of size and internal characteristics.

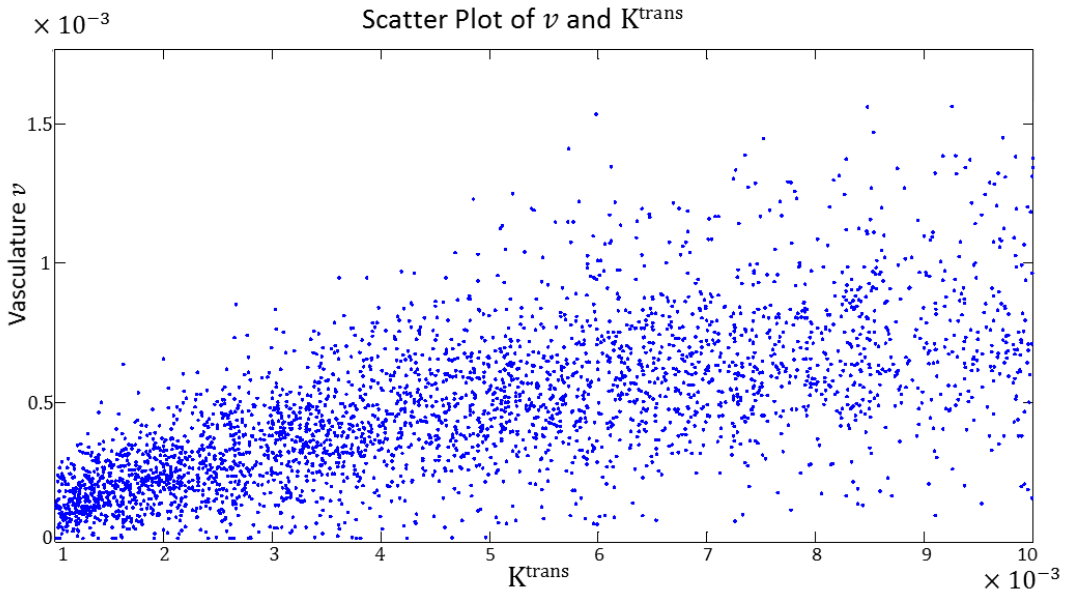

Figure 13_ *Scatterplot of K^{trans} against vasculature.*

PART II

An in silico estimation of the pharmacokinetic profile and the disposition of Gd-DTPA in brain tumor lesions of different vasculature through PBPK models

Brain tumor lesions (BTL), i.e. high grade gliomas, are known to have a prominence of vasculature [18], which is promoted through hypoxia mechanisms and the differential expression of VEGF [1], as described previously. Tracer kinetics plays an important role in DCE-MRI by assessing the vessel leakage through estimation of the transfer and disposition of GBCAs in a lesion. Physiologically-based pharmacokinetic modeling (PBPK) represents a well-documented approach to estimate *in silico* the disposition of pharmacologic agents in the body [66].

In this part, we sought to **1.** estimate the PK profile of Gd-DTPA (Gadopentetic acid, Magnevist®) through a whole-body PBPK approach and **2.** evaluate the impact of vascular fraction of tracer's extravascular-extracellular disposition in a simulated BTL.

PK profile was assessed through the application of Simcyp® simulator platform and the generation of whole-body PBPK model. BTL was introduced as an additional compartment with tissue characteristics matching those of a brain tumor. *In silico* clinical trials (ISCTs) were designed by integrating literature data for a virtual population of patients with cancer for Simcyp® and Gd-DTPA properties. The ISCTs were generated for a representative individual.

This *in silico* approach is capable of assessing the PK profiles of Gd-DTPA and especially its disposition in the EES of a putative BTL.

GD-DTPA IN A SIMULATED BRAIN TUMOR _ METHODS

THE PLATFORM, THE PATIENT AND THE AGENT

Simcyp® platform is a tool for PK-based modelling and simulation which enables drug development predictions with patient variability. The advantage of this method is the ability of applying PBPK modelling for whole-body estimations (figure 20 in APPENDIX). A virtual population of cancer patients profile was used from the Simcyp® simulator platform database [67], while some modifications were chosen regarding hematocrit and plasma proteins. The type of cancer did not matter. The representative individual chosen was the same for all experimental iterations. Demographic information about the subject are given in the table 3.

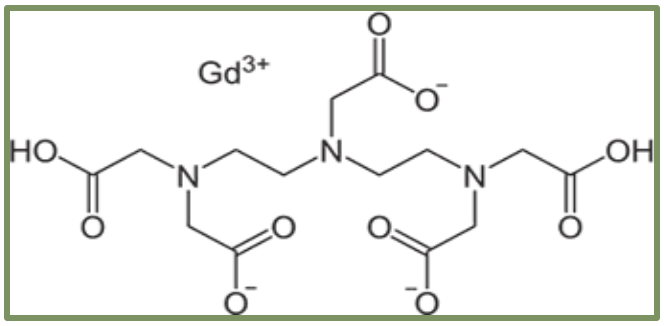

Figure 14_ *Gadopentetic acid, Magnevist®, chemical structure.*

All Gd tracers and Gd-DTPA are hydrophilic (figure 14) and biologically inactive (meaning no pharmacological action) and there is no cell absorption, as explained before. The model was set so as zero intracellular concentration of the tracer is expected in the simulated BTL. BBB's or vessels' permeability to Gd-DTPA was set to be according to its physicochemical characteristics, information provided by the pharmaceutical company. Concentrations were estimated for 15 minutes following i.v. bolus injection of Gd-DTPA (93.8 mg/kg or 0.01mmol/kg).

Table 3 DEMOGRAPHIC DATA OF THE REPRESENTATIVE INDIVIDUAL

Sex	Age (Years)	Weight (kg)	Height (cm)	Brain Weight (g)	Kidney Weight (g)	Liver Weight (g)	Cardiac Output (L/h)	Hematocrit (%)	Renal Function
Male	20	81	177	1391.52	341	1736.96	355.64	43.00	1.13

ADDITIONAL ORGAN AND VASCULATURE PROPORTIONS

The simulated BTL was introduced to the model as an additional organ adopting brain physiology, but lacking BBB. The idea behind this approximation is that we kept the main tissue characteristics stable since the tumor derives from astrocytes and its special features arise from brain physiology, but we removed the BBB, following GBM's hallmarks [3]. In other words, the additional organ is an incorporation of brain and brain tumor characteristics. This new organ has no specific shape or function and its tissue composition is similar to brain in relation to water, lipids and the ratio between extracellular/intracellular water. Anatomically, the volume of the BTL is 6ml which reflects the ~5% of the total brain weight (0.01% of whole body weight) and the cellularity is higher than brain density (~1040g/L), but lower than skin density or bones', around 1300g/L. The previous data were introduced as settings to the simulator platform. In figure 15, there is a visualization of the simulation; a real GBM case from a DCE-MR image juxtaposed with a schematic representation of an *in silico* BTL with characteristics as described above and position in the picture according to the real data. The reason why this MR image was chosen is because of the round-shaped tumor and that the lesion is in the frontal lobe, as most of the demographic elements for GBM [11, 12]. Notice that there is no edema in the picture since the simulator platform does not manage such data.

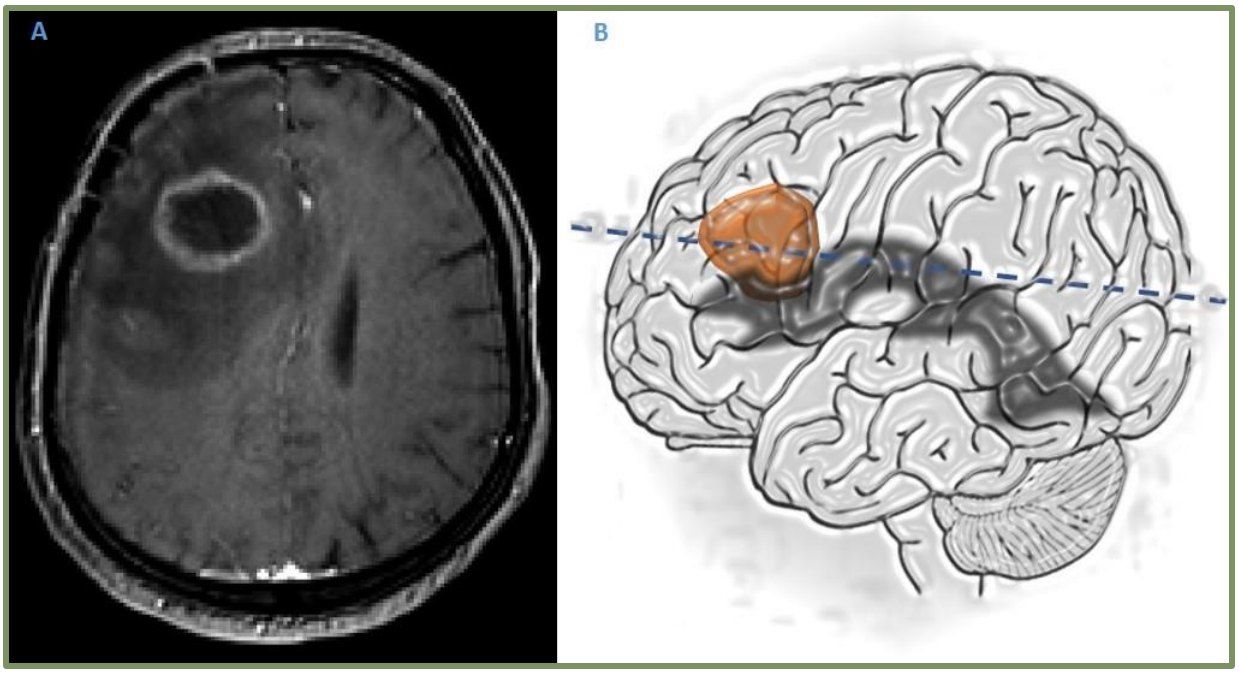

Figure 15_ ***A.*** *T1-weighted MR image (same with figure 4C) with round-shaped GBM in the right frontal lobe and its edema pressing the lateral ventricle;* ***B.*** *Schematic representation of the simulated tumor in a lateral plan view, here displayed with orange, which is supposed to be in the hidden part of the brain in the picture. The simulated tumor was introduced as a shapeless additional organ with brain characteristics, but no BBB. The dark shadow within the brain parenchyma represents the ventricles with the CSF, while the dashed blue line reveals the plane of the axial MRI section on the left.*

The aim of the second part in this work is to evaluate the impact of vasculature proportions in a BTL on the subject of the differential distribution of a Gd tracer. Given the simulated BTL's size, all parameters were kept constant, apart from the proportions of vasculature which are 0.01, 0.1, 0.5, 1, 5, or 10% of the total tissue.

RESULTS AND DISCUSSION

Through this approach, we can determine for the same tumor volume what Gd concentration would reach the tissue if modifying the vasculature portions when taking into account the same perfusion rate every time. It has to be clarified that since brain is a well perfused organ, the Gd distribution rate is primarily determined by permeability [5]. Here, we show that the tracer's concentration within the putative BTL increases as we increase the level of vascularization.

In the following graphs, the contrast agent's plasma concentration, the intra-cranial one and the concentration reaching the simulated BTL through time are presented. What should also be noted is that PBPK models assume that there is tissue homogeneity as regards the vessels' allocation, so as there is no spatial distribution of the Gd and an averaged tissue value is obtained. Moreover, there is no way to introduce to the model non-functional blood vessels, as those described for cancer. In this way, the simulated BTL behaves as the brain regarding blood circulation, but with no BBB.

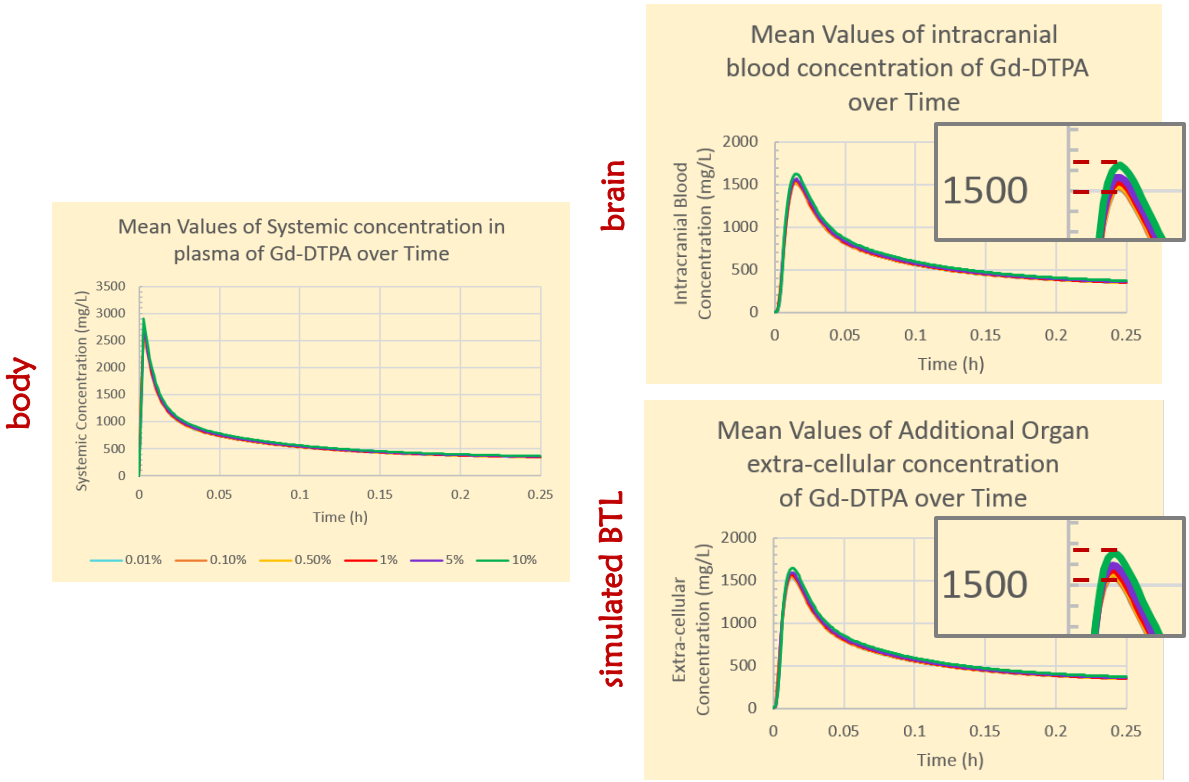

Figure 16_ ***Body:*** *No impact of BTL's vasculature in the whole-body estimations; all series overlap.* ***Brain:*** *As vasculature increases, the intracranial blood concentration also increases.* ***BTL:*** *The extracellular concentration shows a slight enhancement (relative to brain) for different vascular portions, here depicted with different colors.*

Results from the whole-body PBPK simulations estimate the maximum plasma concentration of Gd-DTPA to be ~3.0 mM with no impact of the BTL's differential vasculature portions (figure 16, body). In figure 16, the intracranial blood concentration was estimated to be ~1.5-1.6 mM; this value represents around the 50% of the tracer's systemic concentration. It has to be noted that approximately the 15-20% of the total cardiac output is provided to the brain [68]. There was limited difference between the tracer's distribution

intra-cranially and within the simulated BTL for the different vasculature portions. Regarding the simulated BTL (figure 16, simulated BTL), concentrations varied between 1.5-1.7 mM for the EES following modulation of tissue percentage in capillaries. Alternatively, the tracer's concentration within the BTL increases as we increase vasculature, but not proportionally (figure 17). The tracer's blood concentration existing at the BTL must be approximately equal to the one generally provided to the brain since BTL's vasculature shall be construed as part of the brain's systemic circulation. Finally, zero concentrations are predicted for brain mass and intracellular tissues. As expected, drug penetration to the brain parenchyma is restricted because of the existence of BBB and there is absence of cellular intake, transfer or passive mediated regarding Gd-DTPA.

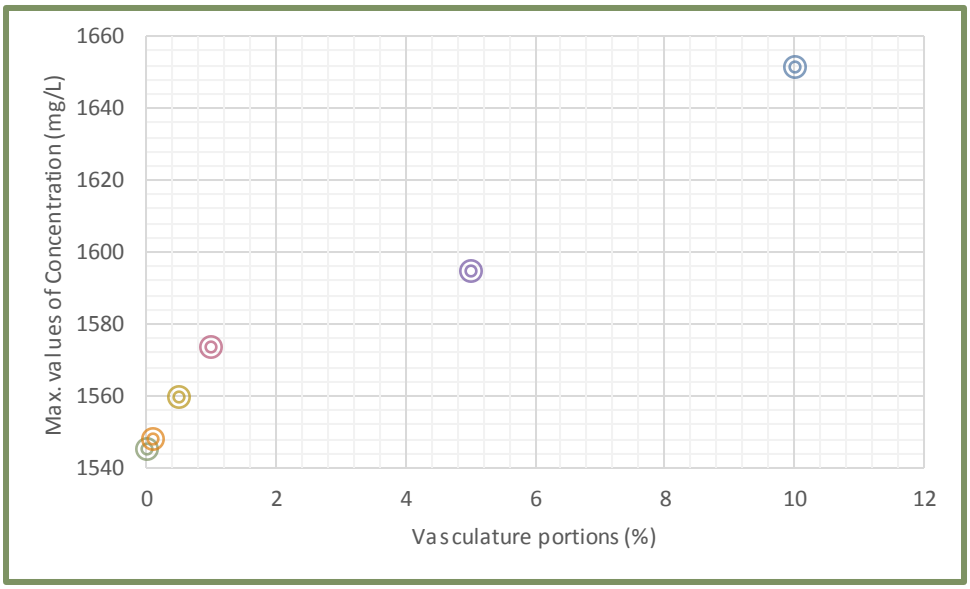

Figure 17_ *There is no linear relationship between the Gd peak concentrations and the vasculature portions. The distribution is strictly increasing.*

GENERAL CONCLUSIONS AND PERSPECTIVES

In this work, the main goal was to provide alternative ways of exploiting DCE-MRI biomarkers applied to computational modeling in terms of utilization in clinical practice. The way that this idea was supported was a function of GBM special characteristics and DCE-MRI rules. A set of assumptions concerning vasculature were suggested in order to be applied accordingly either on a glioma growth model or on a PBPK model. In any case, the purpose was focused on translating imaging data into potentially clinically relevant elements and broadening the individualized application of those models. The main contribution of this work is presented and discussed below.

The first part of our work is an attempt to ameliorate the way of initializing the glioma models by taking into account DCE-MR images from neurologically impaired individuals. DCE-MRI is a plausible clinical examination, while TM is the most common approach for Gd distribution estimations; hence, the significance of translating and subsequently using DCE-MRI to introduce multiple tumor development variables is evident. The main contribution of this assessment is a new way of setting up the different variables (image areas of interest and vasculature) of a glioma model by using biomarkers extracted by DCE-MRI. The assumptions made in relation to K^{trans} represent novel information in this front. The key point is that GBM is a discrete type of cancer. In other words, the assumptions are attributed to GBM's special features which were translated in order to meet model parameters driven by DCE-MRI methodology.

Though two DCE-MR images are the minimum for our implementation, in order to standardize the model parameters there is a need for more validation points per subject and definitely more subjects. To this respect, a sensitivity-specificity analysis, as proposed by [51], would define a range of values within a patient database for the model parameters taken into account. However, there is a difficulty in finding GBM patients without recurrence and/or untreated. Here, the concordance correlation between predictions and real, imaging data shown in the evaluation methods indicate that there is a potential efficiency of the proposed method. However, since this model needs to be validated in a quantitative fashion against more clinical data, the present work can only be considered as a feasibility study.

An alternative prospect is to use additional imaging biomarkers in order to meet other model parameters using either other MRI techniques or PET, Magnetic Resonance Spectroscopic Imaging (MRSI), etc.

As a first step, we oversimplified the discrimination of normoxic and hypoxic areas within the tumor. However, as a future perspective, determining these areas based on K^{trans} and/or other PK parameter values or even additional imaging modalities can be more descriptive and detailed. Alternatively, a control experiment could be used in order to determine the threshold value of K^{trans} in each image area. According to this procedure, a range of values would be assigned to a given area and the ROI divisions could be based on clustering K^{trans} values. This area could be the pituitary gland, a cerebral area with no BBB and characteristics of high oxygen and metabolic demands, similar to the proliferative ring of GBM. If GBM can be considered as a four-compartmentalized region, edema and necrosis can be identified as proposed previously and the normoxic area through the control default bounds. The hypoxic area is the one in between the normoxic and necrotic areas. If this is the case, K^{trans} would not be just translated into vasculature, but the exact discrimination between tumor areas will be based on it.

Finally, as a first approximation, our method was simplified and limited to free tumor growth without treatment. The importance of such patient-specific methods is to have clinical outcome. Thus, the incorporation of therapy effect is crucial. Radiotherapy treatment for example, could be integrated into the model. Using the Linear Quadratic (LQ) model [39, 41] could be in the direction for simulating radiotherapy. The estimation of radiobiology parameters of the LQ is however the most challenging part of this task. Another clinically relevant implementation of our method could be the prediction of a downstaging cancer as a resultant of a wider variety of factors, apart from radiotherapy. If this is the case,

an operable GBM tumor could be identified in time and this would lead to improvement of clinical symptoms.

In the second part of our work, a whole-body PBPK model was used in order to determine the Gd concentration and its PK profile for different vasculature portions (same perfusion rate) of the same tumor volume. A simple notion, the more the Gd concentration the more the vasculature underneath the tissue, was *in silico* proved for a typical cancer patient. The portions of vasculature that were adapted for the additional organ were chosen so as to be representative; counting from really low oxygenation till a marginally over-oxygenated organ. The *in vivo* experiment that was substituted includes multiply scanning the tumor of a certain patient while assuming in the meantime that vasculature grows with tumor upstaging.
The incorporation of PBPK models along with *in silico* tools for tumor growth and/or clinical data could reveal novel approaches for improving DCE-MRI techniques applied in diagnosis and treatment protocols. As a future option, anti-angiogenic drugs (i.e. Avastin®) could be introduced to the model in order to predict treatment efficacy and vasculature changes. Information produced by such execution could be further analyzed and be supplied to glioma models and so on.

Because of the malignancy and the rapid progress, while cognitive and functional deficits are constant as a result of the expanding lesion, in the case of GBM the game that has to be gained is time. In addition, the only tool of GBM diagnosis and FU is imaging techniques and particularly MRI. Thus, the optimal scenario for patients with GBM and brain cancer in general, is to find the right way of decoding MRI scans and obtain knowledge about the specific grade, characteristics, appropriate treatment and patient's response and probability of survival, all these from the very first moment that cancer is diagnosed.

Here, a method for initializing a glioma model based on DCE-MRI biomarkers and an experimental implementation of this method was presented. Moreover, an alternative use of full-PBPK modelling was introduced directed also by DCE-MRI methodology. Individualized predictions to monitor therapeutic effect and tumor development using computational models, with reference to more and more non-invasive imaging biomarkers, should be further investigated targeting direct clinical impact.

ACKNOWLEDGEMENTS

This master thesis reflects both personal effort and combined action of a group of people who should be mentioned. I would like to honestly thank my supervisor **Dr. Kostas Marias** who inspired, organized and contributed to this work and gave me the opportunity to be familiarized in an alternative field of research. Special thanks should also go to **Dr. Vangelis Sakkalis** who was really supportive and his ideas and direction helped me to consolidate both the target and the knowledge. I would also like to thank **Dr. Ioannis Charalampopoulos** who willingly evaluated my theoretical work.

In any case, this work would have never been completed without the contribution of **Dr. Alexandros Roniotis**, who implemented and visualized our results and of **Dr. Eleftheria Tzamali**, who is always there to help, advice and assure the outcome. And off course, all the members of our laboratory, and especially the people I am working with every day, because our partnership gave me ideas and solutions many times, and they contributed to the most creative working conditions. These people are, among others, **Mr. Georgios Grekas, M.Sc.**, who also helped in the implementation of our work, **Mr. Georgios Tzedakis, M.Sc.**, **Ms. Georgia Kanli**, **Mr. Georgios Ioannidis** and **Mr. Konstantinos Spanakis**.

Data of this thesis were successfully and officially exploited.

Part I, which constitutes the main research objective of this work, is ***under submission*** for a journal publication as **"Roniotis, A. and Oraiopoulou, M.E.**, Tzamali, E., Kontopodis, E., Sakkalis, V., Spanakis, M., Van Cauter, S., Marias, K., *A proposed paradigm shift in initializing cancer predictive models with DCE-MRI based PK parameters: A feasibility study"*.

Part II has been presented as a ***poster*** at the 11th European Association of Neuro-Oncology (EANO) meeting, Turin 2014 (presented by **Mariam-Eleni Oraiopoulou**) and also resulted in a ***publication*** cited as "**Spanakis, M.**, **Oraiopoulou, M.E.**, Tzamali, E., Sakkalis, V., Maris, T. G., Papadaki, E., Karantanas, A., Marias, K., *P16.33AN IN SILICO ESTIMATION OF THE PHARMACOKINETIC PROFILE AND THE DISPOSITION OF GD-DTPA IN BRAIN TUMOR LESIONS OF DIFFERENT VASCULATURE THROUGH PBPK MODELS*, Neuro-Oncology, 2014. 16(suppl 2): p. ii85-ii86".

REFERENCES

1. Korkolopoulou, P., et al., *Hypoxia-inducible factor 1alpha/vascular endothelial growth factor axis in astrocytomas. Associations with microvessel morphometry, proliferation and prognosis.* Neuropathol Appl Neurobiol, 2004. **30**(3): p. 267-78.
2. Kleihues, P., et al., *The WHO classification of tumors of the nervous system.* J Neuropathol Exp Neurol, 2002. **61**(3): p. 215-25; discussion 226-9.
3. Ali-Osman, F., *Brain tumors*. Contemporary cancer research. 2005, Totowa, N.J.: Humana Press. xi, 393 p.
4. Goodenberger, M.L. and R.B. Jenkins, *Genetics of adult glioma.* Cancer Genet, 2012. **205**(12): p. 613-21.
5. Schiffer, D., *Brain tumor pathology : current diagnostic hotspots and pitfalls*. 2006, Dordrecht: Springer. vi, 272 p.
6. Goffart, N., J. Kroonen, and B. Rogister, *Glioblastoma-initiating cells: relationship with neural stem cells and the micro-environment.* Cancers (Basel), 2013. **5**(3): p. 1049-71.
7. Flynn, J.R., et al., *Hypoxia-regulated protein expression, patient characteristics, and preoperative imaging as predictors of survival in adults with glioblastoma multiforme.* Cancer, 2008. **113**(5): p. 1032-42.
8. Lee, E.J., et al., *Potential role of advanced MRI techniques for the peritumoural region in differentiating glioblastoma multiforme and solitary metastatic lesions.* Clin Radiol, 2013. **68**(12): p. e689-97.
9. Tsougos, I., et al., *Differentiation of glioblastoma multiforme from metastatic brain tumor using proton magnetic resonance spectroscopy, diffusion and perfusion metrics at 3 T.* Cancer Imaging, 2012. **12**: p. 423-36.
10. Fonkem, E., M. Lun, and E.T. Wong, *Rare phenomenon of extracranial metastasis of glioblastoma.* J Clin Oncol, 2011. **29**(34): p. 4594-5.
11. Krex, D., et al., *Long-term survival with glioblastoma multiforme.* Brain, 2007. **130**(Pt 10): p. 2596-606.
12. Zada, G., et al., *Incidence trends in the anatomic location of primary malignant brain tumors in the United States: 1992-2006.* World Neurosurg, 2012. **77**(3-4): p. 518-24.
13. Hou, L.C., et al., *Recurrent glioblastoma multiforme: a review of natural history and management options.* Neurosurg Focus, 2006. **20**(4): p. E5.
14. McNamara, M.G., S. Sahebjam, and W.P. Mason, *Emerging biomarkers in glioblastoma.* Cancers (Basel), 2013. **5**(3): p. 1103-19.
15. Fraisl, P., et al., *Regulation of angiogenesis by oxygen and metabolism.* Dev Cell, 2009. **16**(2): p. 167-79.
16. Potente, M., H. Gerhardt, and P. Carmeliet, *Basic and therapeutic aspects of angiogenesis.* Cell, 2011. **146**(6): p. 873-87.
17. Carmeliet, P., *Mechanisms of angiogenesis and arteriogenesis.* Nat Med, 2000. **6**(4): p. 389-95.
18. Hardee, M.E. and D. Zagzag, *Mechanisms of glioma-associated neovascularization.* Am J Pathol, 2012. **181**(4): p. 1126-41.
19. Soda, Y., et al., *Mechanisms of neovascularization and resistance to anti-angiogenic therapies in glioblastoma multiforme.* J Mol Med (Berl), 2013. **91**(4): p. 439-48.
20. Ellingson, B.M., et al., *Pretreatment ADC Histogram Analysis Is a Predictive Imaging Biomarker for Bevacizumab Treatment but Not Chemotherapy in Recurrent Glioblastoma.* AJNR Am J Neuroradiol, 2013.
21. Pope, W.B., et al., *Differential gene expression in glioblastoma defined by ADC histogram analysis: relationship to extracellular matrix molecules and survival.* AJNR Am J Neuroradiol, 2012. **33**(6): p. 1059-64.
22. Elens, I., *Clinical Study: Resection and Immunotherapy for Recurrent Grade III*

Glioma. ISRN Immunology, 2012. **2012** (2012): p. 1-9.

23. Horska, A. and P.B. Barker, *Imaging of brain tumors: MR spectroscopy and metabolic imaging.* Neuroimaging Clin N Am, 2010. **20**(3): p. 293-310.

24. Atuegwu, N.C., et al., *Parameterizing the Logistic Model of Tumor Growth by DW-MRI and DCE-MRI Data to Predict Treatment Response and Changes in Breast Cancer Cellularity during Neoadjuvant Chemotherapy.* Transl Oncol, 2013. **6**(3): p. 256-64.

25. Yankeelov, T.E., et al., *Clinically relevant modeling of tumor growth and treatment response.* Sci Transl Med, 2013. **5**(187): p. 187ps9.

26. Hagmann, P., et al., *Understanding diffusion MR imaging techniques: from scalar diffusion-weighted imaging to diffusion tensor imaging and beyond.* Radiographics, 2006. **26 Suppl 1**: p. S205-23.

27. Turkbey, B., et al., *Imaging of tumor angiogenesis: functional or targeted?* AJR Am J Roentgenol, 2009. **193**(2): p. 304-13.

28. Maitland, M.L., et al., *Vascular endothelial growth factor pathway.* Pharmacogenet Genomics, 2010. **20**(5): p. 346-9.

29. Ferrara, N., K.J. Hillan, and W. Novotny, *Bevacizumab (Avastin), a humanized anti-VEGF monoclonal antibody for cancer therapy.* Biochem Biophys Res Commun, 2005. **333**(2): p. 328-35.

30. Zustovich, F., et al., *Bevacizumab as front-line treatment of brain metastases from solid tumors: a case series.* Anticancer Res, 2013. **33**(9): p. 4061-5.

31. Leach, M.O., et al., *The assessment of antiangiogenic and antivascular therapies in early-stage clinical trials using magnetic resonance imaging: issues and recommendations.* Br J Cancer, 2005. **92**(9): p. 1599-610.

32. Pope, W.B., et al., *Recurrent glioblastoma multiforme: ADC histogram analysis predicts response to bevacizumab treatment.* Radiology, 2009. **252**(1): p. 182-9.

33. Pope, W.B., et al., *Apparent diffusion coefficient histogram analysis stratifies progression-free survival in newly diagnosed bevacizumab-treated glioblastoma.* AJNR Am J Neuroradiol, 2011. **32**(5): p. 882-9.

34. Lee, E.J., et al., *Diagnostic value of peritumoral minimum apparent diffusion coefficient for differentiation of glioblastoma multiforme from solitary metastatic lesions.* AJR Am J Roentgenol, 2011. **196**(1): p. 71-6.

35. Zaman, M.H., et al., *Migration of tumor cells in 3D matrices is governed by matrix stiffness along with cell-matrix adhesion and proteolysis.* Proc Natl Acad Sci U S A, 2006. **103**(29): p. 10889-94.

36. Hatzikirou, H. and A. Deutsch, *Cellular Automata as Microscopic Models of Cell Migration in Heterogeneous Environments*, in *Current Topics in Developmental Biology*, P.K.M.S.A.N. Santiago Schnell and J.N. Timothy, Editors. 2008, Academic Press. p. 401-434.

37. Lowengrub, J.S., et al., *Nonlinear modelling of cancer: bridging the gap between cells and tumours.* Nonlinearity, 2010. **23**(1): p. R1.

38. Stamatakos, G.S., et al., *A four-dimensional computer simulation model of the in vivo response to radiotherapy of glioblastoma multiforme: studies on the effect of clonogenic cell density.* Br J Radiol, 2006. **79**(941): p. 389-400.

39. Roniotis, A., et al., *Simulating radiotherapy effect in high-grade glioma by using diffusive modeling and brain atlases.* J Biomed Biotechnol, 2012. **2012**: p. 715812.

40. Clatz, O., et al., *Realistic simulation of the 3-D growth of brain tumors in MR images coupling diffusion with biomechanical deformation.* IEEE Trans Med Imaging, 2005. **24**(10): p. 1334-46.

41. Jbabdi, S., et al., *Simulation of anisotropic growth of low-grade gliomas using diffusion tensor imaging.* Magn Reson Med, 2005. **54**(3): p. 616-24.

42. Swanson, K.R., E.C. Alvord, Jr., and J.D. Murray, *A quantitative model for differential motility of gliomas in grey and white matter.* Cell Prolif, 2000. **33**(5): p. 317-29.

43. Roniotis, A., et al., *In-depth analysis and evaluation of diffusive glioma models.* IEEE Trans Inf Technol Biomed, 2012. **16**(3): p. 299-307.

44. Roniotis, A., et al., *High-grade glioma diffusive modeling using statistical tissue information and diffusion tensors extracted from atlases.* IEEE Trans Inf Technol Biomed, 2012. **16**(2): p. 255-63.

45. Baldock, A.L., et al., *From patient-specific mathematical neuro-oncology to precision medicine.* Front Oncol, 2013. **3**: p. 62.

46. Tofts, P.S. and A.G. Kermode, *Measurement of the blood-brain barrier permeability and leakage space using dynamic MR imaging. 1. Fundamental concepts.* Magn Reson Med, 1991. **17**(2): p. 357-67.

47. Swanson, K.R., R.C. Rostomily, and E.C. Alvord, Jr., *A mathematical modelling tool for predicting survival of individual patients following resection of glioblastoma: a proof of principle.* Br J Cancer, 2008. **98**(1): p. 113-9.

48. Ellingson, B.M., et al., *Spatially quantifying microscopic tumor invasion and proliferation using a voxel-wise solution to a glioma growth model and serial diffusion MRI.* Magn Reson Med, 2011. **65**(4): p. 1131-43.

49. Szeto, M.D., et al., *Quantitative metrics of net proliferation and invasion link biological aggressiveness assessed by MRI with hypoxia assessed by FMISO-PET in newly diagnosed glioblastomas.* Cancer Res, 2009. **69**(10): p. 4502-9.

50. Swanson, K.R., et al., *Complementary but distinct roles for MRI and 18F-fluoromisonidazole PET in the assessment of human glioblastomas.* J Nucl Med, 2009. **50**(1): p. 36-44.

51. Swanson, K.R., et al., *Quantifying the role of angiogenesis in malignant progression of gliomas: in silico modeling integrates imaging and histology.* Cancer Res, 2011. **71**(24): p. 7366-75.

52. Hinow, P., et al., *A spatial model of tumor-host interaction: application of chemotherapy.* Math Biosci Eng, 2009. **6**(3): p. 521-46.

53. Tzamali, E., et al., *Employing in-vivo molecular imaging in simulating and validating tumor growth.* Conf Proc IEEE Eng Med Biol Soc, 2013. **2013**: p. 5533-6.

54. Zetter, B.R., *The scientific contributions of M. Judah Folkman to cancer research.* Nat Rev Cancer, 2008. **8**(8): p. 647-54.

55. Daub, J.T. and R.M. Merks, *A cell-based model of extracellular-matrix-guided endothelial cell migration during angiogenesis.* Bull Math Biol, 2013. **75**(8): p. 1377-99.

56. Mammoto, T., et al., *Role of collagen matrix in tumor angiogenesis and glioblastoma multiforme progression.* Am J Pathol, 2013. **183**(4): p. 1293-305.

57. Hanahan, D. and R.A. Weinberg, *Hallmarks of cancer: the next generation.* Cell, 2011. **144**(5): p. 646-74.

58. Wachspress, E.L. and G.J. Habetler, *An Alternating-Direction-Implicit Iteration Technique.* J. Soc. Indust. Appl. Math., 1960. **8**(2): p. 403–423.

59. Douglas, J.J., *Alternating direction methods for three space variables.* Numerische Mathematik, 1962. **4**(1): p. 41-63

60. Batista, C.M., et al., *Adult Neurogenesis and Glial Oncogenesis: When the Process Fails.* BioMed Research International, 2014. **2014**: p. 10.

61. Jackson, A., et al., *Imaging tumor vascular heterogeneity and angiogenesis using dynamic contrast-enhanced magnetic resonance imaging.* Clin Cancer Res, 2007. **13**(12): p. 3449-59.

62. Freyer, J.P. and R.M. Sutherland, *Regulation of growth saturation and development of necrosis in EMT6/Ro multicellular spheroids by the glucose and oxygen supply.* Cancer Res, 1986. **46**(7): p. 3504-12.

63. Mueller-Klieser, W., *Method for the determination of oxygen consumption rates and diffusion coefficients in multicellular spheroids.* Biophys J, 1984. **46**(3): p. 343-8.

64. Freyer, J.P. and R.M. Sutherland, *Proliferative and clonogenic heterogeneity of cells from EMT6/Ro multicellular spheroids*

induced by the glucose and oxygen supply. Cancer Res, 1986. **46**(7): p. 3513-20.

65. Hegedus, B., et al., *Locomotion and proliferation of glioblastoma cells in vitro: statistical evaluation of videomicroscopic observations.* J Neurosurg, 2000. **92**(3): p. 428-34.

66. Barboriak, D.P., et al., *Comparison of three physiologically-based pharmacokinetic models for the prediction of contrast agent distribution measured by dynamic MR imaging.* J Magn Reson Imaging, 2008. **27**(6): p. 1388-98.

67. Cheeti, S., et al., *A physiologically based pharmacokinetic (PBPK) approach to evaluate pharmacokinetics in patients with cancer.* Biopharm Drug Dispos, 2013. **34**(3): p. 141-54.

68. McCorry, L.K., *Essentials of human physiology for pharmacy*. 2nd ed. CRC Press pharmacy education series. 2009, Boca Raton: CRC Press/Taylor & Francis. xx, 496 p.

69. Wen, P.Y., et al., *Updated response assessment criteria for high-grade gliomas: response assessment in neuro-oncology working group.* J Clin Oncol, 2010. **28**(11): p. 1963-72.

70. Pope, W.B., J.R. Young, and B.M. Ellingson, *Advances in MRI assessment of gliomas and response to anti-VEGF therapy.* Curr Neurol Neurosci Rep, 2011. **11**(3): p. 336-44.

APPENDIX

Table 4 RESPONSE ASSESSMENT CRITERIA IN NEURO-ONCOLOGY (RANO) FOR HIGH-GRADE GLIOMAS TAKING INTO ACCOUNT IMAGE ANALYSIS AND CLINICAL DATA [ADOPTED FROM [69, 70]]

Response	*Criteria*
Complete response	*Requires all of the following:* • *Disappearance of all enhancing measurable and non-measurable disease sustained for a minimum of 4 weeks* • *Stable or improved FLAIR/T2 lesions* • *No new lesions* • *Clinical status is stable or improved* • *Patients cannot be receiving corticosteroids (physiologic replacement doses are acceptable)*
Partial response	*Requires all of the following:* • *50%or greater decrease (compared with baseline) in the sum of products of perpendicular diameters of all measurable enhancing lesions sustained for a minimum of 4 weeks* • *No progression of non-measurable disease* • *No new lesions* • *Stable or improved FLAIR/T2 lesions* • *Clinical status is stable or improved* • *The corticosteroid dosage at the time of the scan should be no greater than the dosage at the time of the baseline scan*
Stable disease	*Requires all of the following:* • *Patient does not qualify for complete response, partial response, or progression* • *Stable FLAIR/T2 lesions on a corticosteroid dose no greater than at baseline* • *Clinical status is stable*
Progression	*Defined by any of the following:* • *25% or greater increase in sum of the products of perpendicular diameters of all measurable enhancing lesions compared with the smallest tumor measurement obtained either at baseline or best response following the initiation of therapy, while on a stable or increasing dose of corticosteroids.* • *Significant increase in FLAIR/T2 lesions compared with baseline or best response following initiation of therapy, not caused by comorbid events (e.g., radiation therapy, ischemic injury, seizures, postoperative changes, or other treatment effects), while on a stable or increasing dose of corticosteroids* • *Presence of new lesions* • *Clinical deterioration not attributable to other causes apart from the tumor (e.g., seizures, medication side effects, complications of therapy, cerebrovascular events, infection) or decreases in corticosteroid dose* • *Failure to return for evaluation due to death or deteriorating condition* • *Clear progression of non-measurable disease*

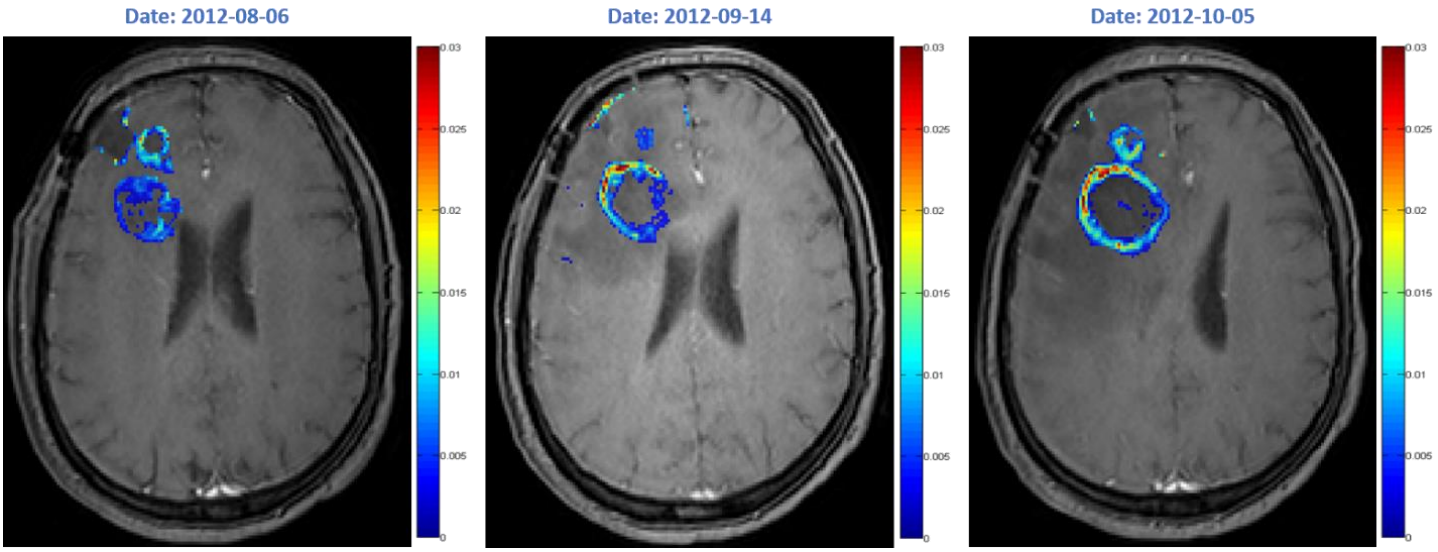

Figure 18_ *The three DCE-MR images; the diagnostic and the two FUs sessions. The FU2 was not used in our approximation as a second validation point.*

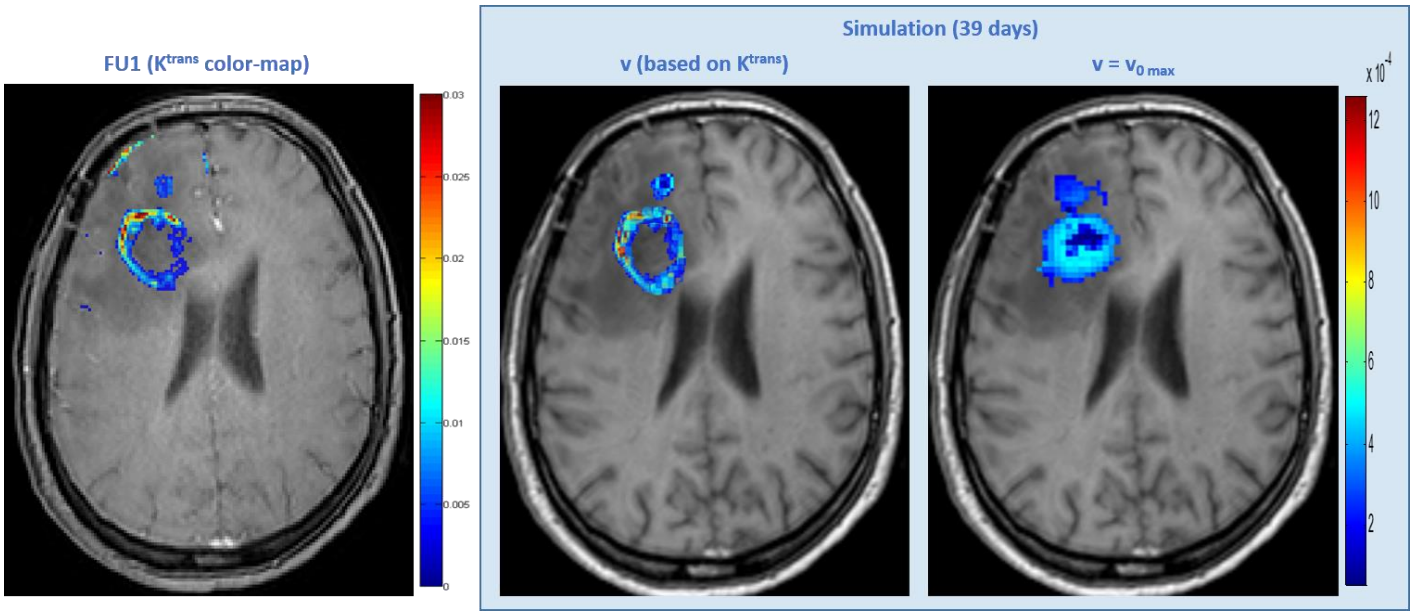

Figure 19_ *The simulated vasculature after 39 days either based on K^{trans} initialization as described above or using a uniform v initialization with a maximum value.* ***Left:*** *The real ktrans map of FU1 used as a validation point. As it can be seen, when v is set based on K^{trans} the simulated image resembles that of real data.*

Extend of normoxic area (c)	Parameters	Jaccard Similarity	Dice Similarity	Volume Similarity
Erosion 1mm	ρ=0.06931, D=3.6e^{-8}	92.06%	94.57%	97.67%
	0.1D	74.81%	77.35%	79.21%
	10D	87.17%	89.64%	91.02%
	0.1ρ	79.11%	84.57%	85.83%
	10ρ	86.44%	89.93%	92.31%
	10ρ AND 0.1D	59.65%	60.98%	64.21%
	uniform v	34.67%	41.77%	43.52%
Erosion 5mm	ρ, D	72.47%	73.12%	72.04%
Erosion 10mm	ρ, D	33.01%	34.17%	35.12%

TABLE 5 METRICS FOR v

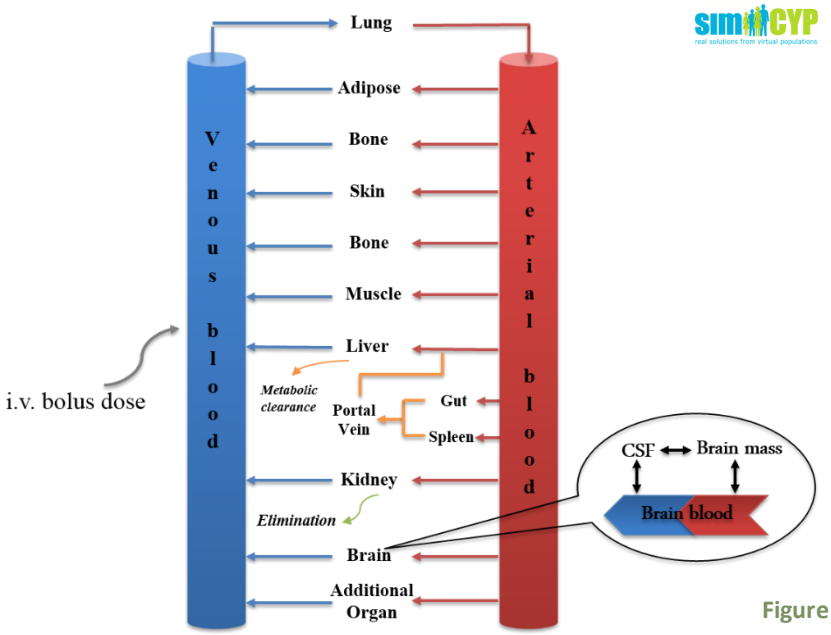

Figure 20_ A *whole-body PBPK model.*